Published in final edited form as:
Cell Rep. 2019 June 25; 27(13): 3939–3955.e6. doi:10.1016/j.celrep.2019.05.092.

Glucose Metabolism Drives Histone Acetylation Landscape Transitions that Dictate Muscle Stem Cell Function

Nora Yucel[1,4], **Yu Xin Wang**[1,4], **Thach Mai**[1], **Ermelinda Porpiglia**[1], **Peder J. Lund**[2], **Glenn Markov**[1], **Benjamin A. Garcia**[2], **Sean C. Bendall**[3], **Michael Angelo**[3], **Helen M. Blau**[1,5,*]

[1]Baxter Laboratory for Stem Cell Biology, Department of Microbiology and Immunology, Institute for Stem Cell Biology and Regenerative Medicine, Stanford University School of Medicine, Stanford, CA 94305, USA

[2]Perelman School of Medicine, University of Pennsylvania, Philadelphia, PA, USA

[3]Department of Pathology, Stanford University, Stanford, CA, USA

[4]These authors contributed equally

[5]Lead Contact

SUMMARY

The impact of glucose metabolism on muscle regeneration remains unresolved. We identify glucose metabolism as a crucial driver of histone acetylation and myogenic cell fate. We use single-cell mass cytometry (CyTOF) and flow cytometry to characterize the histone acetylation and metabolic states of quiescent, activated, and differentiating muscle stem cells (MuSCs). We find glucose is dispensable for mitochondrial respiration in proliferating MuSCs, so that glucose becomes available for maintaining high histone acetylation via acetyl-CoA. Conversely, quiescent and differentiating MuSCs increase glucose utilization for respiration and have consequently reduced acetylation. Pyruvate dehydrogenase (PDH) activity serves as a rheostat for histone acetylation and must be controlled for muscle regeneration. Increased PDH activity in proliferation increases histone acetylation and chromatin accessibility at genes that must be silenced for differentiation to proceed, and thus promotes self-renewal. These results highlight metabolism as a determinant of MuSC histone acetylation, fate, and function during muscle regeneration.

Graphical Abstract

---

[*]Correspondence: hblau@stanford.edu.

AUTHOR CONTRIBUTIONS

N.Y. and H.M.B. designed experiments. N.Y., E.P., M.A., and S.C.B. designed and constructed CyTOF antibody panel. Fiber isolations and staining were performed by Y.X.W. ChIP experiments and *in silico* analysis of ENCODE ChIP-sequencing data were performed by T.M. and Y.X.W. ATAC-seq experiments and analysis were performed by Y.X.W. and G.M. Bulk histone mass spectrometry preparation and analyses were conducted by P.J.L. in the laboratory of B.A.G. All other experiments and analyses were performed by N.Y. Manuscript was prepared by N.Y., Y.X.W., and H.M.B. with input from all authors.

SUPPLEMENTAL INFORMATION

Supplemental Information can be found online at https://doi.org/10.1016/j.celrep.2019.05.092.

DECLARATIONS OF INTEREST

The authors declare no competing interests.

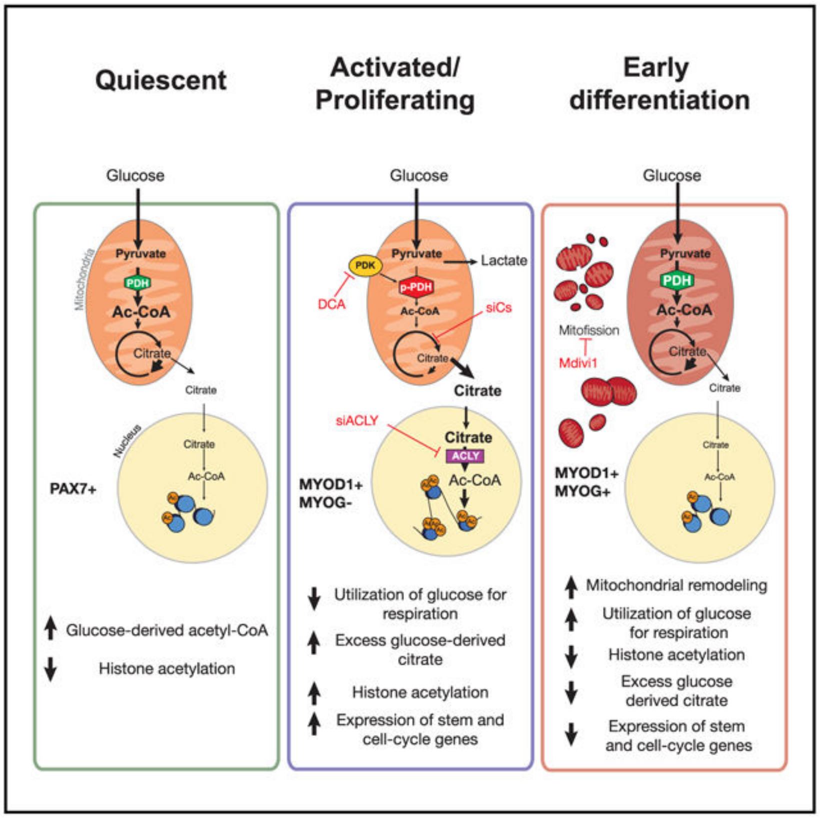

In Brief

Yucel et al. identify a link between stem cells' metabolism and their fate and function. Mitochondrial glucose utilization determines remodeling of the histone acetylation landscape of muscle stem cells during tissue regeneration. Pyruvate dehydrogenase (PDH) is a pivotal control point for this and determines the differentiation potential of myogenic progenitors.

INTRODUCTION

Skeletal muscle is a central metabolic organ. It comprises ~40% of body mass in mammals, 50%–75% of all protein, accounts for ~30% of the resting metabolic rate, and serves as the primary site (~80%) of post-prandial glucose uptake (Rasmussen and Phillips, 2003; Zurlo et al., 1990). Despite the role of muscle in glucose homeostasis, little is known about the impact of glucose metabolism on muscle regeneration.

Muscle stem cells (MuSCs), or satellite cells, are critical for the regeneration of skeletal muscle, and for maintaining muscle mass in adult tissues (Brack et al., 2005; Collins et al., 2005; Fry et al., 2015; Lepper et al., 2011; Sambasivan et al., 2011; Tanaka et al., 2009). In homeostasis, MuSCs are largely quiescent and characterized by the expression of the transcription factor PAX7 (Seale et al., 2000; von Maltzahn et al., 2013). Upon injury, MuSCs are activated, and transiently expand as proliferating MuSCs (or myoblasts), which express the transcription factor MYOD1 (Cooper et al., 1999; Megeney et al., 1996). As regeneration completes, MuSCs exit cell cycle to become differentiating progenitors characterized by the transcription factor Myogenin (MYOG) (Wright et al., 1989). Differentiating progenitors fuse to form new myofibers that express mature myosin heavy-chain isoforms (Silberstein et al., 1986). Intrinsic and extrinsic regulators of myogenesis during adult muscle regeneration have been identified, including biophysical, extracellular matrix, and molecular signaling factors. However, our understanding of the metabolic cues that regulate MuSC function during regeneration remains limited (Cerletti et al., 2012; Pala et al., 2018; Ryall et al., 2015; Tang and Rando, 2014). Here, we identify glucose metabolism as a crucial mediator of epigenetic landscape during MuSC fate transitions.

Epigenetic landscape, or the pattern of histone modifications that dictates DNA accessibility, is a determinant of cell identity. Of these modifications, histone lysine acetylation marks open chromatin and active gene expression. It is dynamically regulated by histone acetyl-transferases (HATs) and histone deacetylases (HDACs), as well as availability of acetyl-CoA, the eponymous substrate for HATs (Choudhary et al., 2014; Moussaieff et al., 2015; Wellen et al., 2009). Glucose has been shown to be a major source for histone acetylation (Evertts et al., 2013; Wellen et al., 2009), via the pyruvate dehydrogenase complex (PDH) in the mitochondria, which converts pyruvate to acetyl-CoA. Acetyl-CoA is then converted to citrate by citrate synthase (CS), which can be used in the tricarboxylic acid (TCA) cycle. Unused citrate can be transported out of the mitochondria and diffuse into the nucleus, where it is cleaved by ATP-citrate lyase (ACLY) to reform acetyl-CoA, which is used to acetylate histones. Consequently, glucose metabolism via PDH and ACLY is a regulator of the histone acetylation state.

Here, we use mass cytometry (CyTOF) (Bendall et al., 2011; Porpiglia et al., 2017) and flow cytometry to identify distinct histone acetylation states characteristic of quiescence, proliferation, and differentiation of MuSCs. We characterize distinct histone acetylation states in conjunction with metabolic signatures that mark these MuSC states. We show that low utilization of glucose for mitochondrial respiration in proliferating MuSCs leads to increased available acetyl-CoA and, in turn, elevated histone acetylation. In this state, PDH acts as a metabolic rheostat for glucose-derived histone acetylation. During differentiation, mitochondrial remodeling and increased reliance on glucose to support respiration restricts glucose-derived histone acetylation, resulting in a decreased histone acetylation that precedes MYOG. Increasing PDH activity results in elevation of histone acetylation and reduced differentiation capacity both in vitro and in vivo. Finally, we use chromatin immunoprecipitation (ChIP) and assay for transposase accessible chromatin (ATAC) followed by sequencing to characterize the effects of glucose-derived acetyl-CoA on the epigenetic landscape. We find that glucose-derived histone acetylation regulates chromatin accessibility at genes that must be turned off for differentiation. Thus, we identify metabolic regulation of histone acetylation state as a crucial component of myogenesis that acts in coordination with the canonical myogenic program.

RESULTS

Single-Cell Analysis Reveals Distinct Histone Acetylation States during Regeneration

We sought to identify global changes in histone acetylation in MuSCs during regeneration. To understand cellular heterogeneity, we analyzed histone acetylation state in single cells by

CyTOF. CyTOF enables simultaneous analysis of MuSCs and progenitor cells during muscle regeneration (Porpiglia et al., 2017) concurrent with a range of well-studied histone acetylation marks (H3K9, H3K18, H4K16, and H2BK5) (Feller et al., 2015; Young et al., 2009). *Tibialis anterior* (TA) and *gastrocnemius* (GAS) muscles were collected in uninjured animals or 6 days following injury by notexin injection (Figures 1A-1D). MuSCs and progenitors were gated for absence of blood and endothelial cell lineage markers (Lin$^-$: Sca1, CD11b, CD45, CD31) and the presence of α7-integrin$^+$ (Figure S1A), as well as expression of the quiescence marker CD34, and transcription factors PAX7, MYOD1, or MYOG. Myogenic cells were classified as (1) quiescent PAX7$^+$CD34$^+$MYOD$^-$ MuSCs from uninjured samples; (2) self-renewing PAX7$^+$CD34$^-$MYOD$^-$ MuSCs from injured samples; (3) activated PAX7$^+$CD34$^-$MYOD$^+$ MuSCs from injured samples; and (4) differentiating PAX7$^-$MYOD1$^+$MYOG$^+$ progenitors from injured samples (Figures 1A, 1B, and S1B). Self-renewing PAX7$^+$MYOD$^-$ MuSCs have been shown to repopulate the stem cell pool, while committed activated MuSCs that express MYOD go on to differentiate (Shea et al., 2010). All injured populations had ~15%–25% iododeoxyuridine (IdU) incorporation, while quiescent MuSCs were IdU negative, suggesting that self-renewing PAX7$^+$CD34$^-$MYOD$^-$ MuSCs are distinct from quiescent MuSCs in resting muscle (Figure 1C).

We identified distinct histone acetylation states in MuSCs in uninjured and injured tissue. Activated PAX7$^+$ (MYOD$^-$ and MYOD$^+$) MuSCs, from injured samples, had elevated acetylation on H3K9, H4K16, and H2BK5 compared to uninjured quiescent PAX7$^+$ MuSCs (Figures 1C and 1D). In contrast, PAX7$^-$MYOG$^+$ differentiating progenitors had reduced acetylation on all marks (H3K9, H3K18, H4K16, and H2BK5) compared to PAX7$^+$MYOD$^+$ activated MuSCs. These histone acetylation patterns were also observed by flow cytometric analysis, using CD34 and MYOG as markers to identify quiescent, activated, and differentiating subsets (Figures 1E, 1F, S1C, and S1D). Qualitatively, acetylation changes were apparent by immunofluorescence of single quiescent (PAX7$^+$MYOD$^-$), activated (PAX7$^+$MYOD$^+$) MuSCs, and differentiating progenitors (PAX7$^-$MYOD$^+$ or MYOD$^+$MYOG$^+$) on freshly isolated and cultured myofibers (Figures 1G and S2A-S2C). Notably, by immunofluorescence, histone acetylation was barely perceptible in quiescent MuSCs, except for H3K18. This increased baseline could explain why for H3K18 acetylation is not further increased with activation (Figure S2B). These data demonstrate that changes in histone acetylation state accompany transitions in myogenic stem cell states *in vitro* and *in vivo*.

General Reduction in Histone Acetylation during Early Myogenic Differentiation

We were struck by the reduction in histone acetylation in MYOG$^+$ progenitors. This decrease in histone acetylation agrees with previous chromatin immunoprecipitation sequencing (ChIP-seq) studies, which have shown loss of acetylation on histones H3K9, H3K18, H4K12, and H3K27 in fully differentiated myotubes (Asp et al., 2011; Blum and Dynlacht, 2013). However, studies have also shown that histone acetylation of myogenic genes increases during differentiation (Francetic et al., 2012; Hamed et al., 2013; Iezzi et al., 2002, 2004). Therefore, we sought to reconcile and characterize the interplay between these two phenomena.

To eliminate confounding effects of serum withdrawal, we analyzed primary myoblasts, i.e., MuSCs isolated by fluorescence-activated cell sorting (FACS), cultured to confluency in high serum growth media (GM), which induces differentiation in a subset of cells. Using flow cytometry, we compared histone acetylation in MYOG$^-$ versus MYOG$^+$ myoblasts in these heterogeneous cultures (Figures 2A and S3A). We also assayed histone acetylation in undifferentiated, sub-confluent myoblasts in GM versus confluent myoblasts after induction of differentiation for 24 h in low serum differentiation media (DM). After 24 h in DM, 30%–60% of myoblasts were positive for MYOG$^+$ (Figures S3B and S3C). Histone acetylation marks were examined by flow cytometry in MYOG$^+$ and MYOG$^-$ cells (Figure 2B). In agreement with analyses of regenerating muscle, we observed reduced acetylation of all marks in MYOG$^+$ compared to MYOG$^-$ cells. Similarly, myoblasts differentiated in DM for 24 h had reduced histone acetylation compared to those in GM. Notably, after 24 h in DM, both MYOG$^+$ and MYOG$^-$ myoblasts had reduced histone acetylation compared to cells in GM (Figure 2C). These data demonstrate that loss of histone acetylation is associated with early myogenic differentiation and precedes MYOG expression.

In order to quantitatively measure histone acetylation without antibody bias, we performed liquid chromatography mass spectrometry (LC-MS/MS) to detect histone acetylation in sub-confluent myoblasts in GM versus early differentiating myoblasts in DM (24 h). Acetylation was detected as relative abundance, or the fraction of each histone peptide that contained one or more acetylated lysine residues. Acetylation was quantified for peptides corresponding to histone 3 lysines 9 and 14 (H3K9|14), histone 3 lysines 18 and 23 (H3K18|23), histone 4 lysines 5, 8, 12, and 16 (H4K5|8|12|16), and histone 2 variant A.1 lysine 5 and 9 (H2A.1K5|9), respectively. Notably, acetylation of histone 2B, as well as histone H3 lysine 27 and lysine 56, was not detected at a reliable rate by this assay and was not included in subsequent analysis. We observed a decrease in mono acetylation at H3K9|14 (−27.5%), H3K18|23 (−12.8%), and H4K5|8|12|16 (−5%; $p = 0.0659$) (Figure 2D). In addition, we identified a decrease in the acetylation of H2A.1K5 (−37%) and the di- and tri-acetylated state of H4K5|8|12|16 (−12.6% and −10.4%, respectively). In agreement with our antibody-based findings by CyTOF and flow cytometry, these results confirmed that histone acetylation loss at these lysine residues is occurring independent of histone tail cleavage or changes in histone variants.

Site-Specific Histone Acetylation Changes

Histone acetylation is generally considered a mark of open chromatin that occurs at the enhancers or transcriptional start sites (TSSs) of transcriptionally active or poised genes (Taylor et al., 2013; Wang et al., 2008). We sought to reconcile the global loss of histone acetylation with the known increase in histone acetylation at the promoters of myogenic genes during differentiation. To this end, we analyzed available ChIP-sequencing data of H3K9|14 in C2C12 myoblasts and 24 h after induction of differentiation in DM (ENCODE, GSE36023) and H3K9, H3K18, H4K12, and H3K27 acetylation in C2C12 myoblasts versus myotubes (differentiated 7 days) (Asp et al., 2011; Blum and Dynlacht, 2013). Analysis of ENCODE data showed a global decrease in acetylation occurs at 24 h of differentiation in agreement with our findings (Figure 2E). In all data, this decrease occurs not only on genes that decrease expression, as expected, but also on average over genes that do not change, or those that increase expression. Analysis of these ChIP-sequencing data showed that, in total, 8,963 genes have associated ChIP peaks with decreased acetylation on one or more marks following differentiation. Genes with decreased histone acetylation on any one mark were enriched (1.3- to 1.94-fold) for chromatin remodeling, cell cycle, and metabolic processes. In contrast, increased acetylation was much more restricted. Only 1,987 genes had increased acetylation on one or more mark, and an even fewer 105 genes had associated peaks that showed increased acetylation on three or more marks (Figure 2F). Genes associated with peaks that increased histone acetylation were strongly enriched (up to 14-fold) for muscle specification and development, including myogenic differentiation factors *Myog*, *Mef2c*, and various *Myh* genes. We confirmed these results by ChIP-qPCR of H3K9|14 for a subset of genes in primary myoblasts 24 h after induction of differentiation (Figure S3D). Although on average histone acetylation was reduced, gain or loss of histone acetylation was concordant with changes in mRNA expression for a number of genes (Figure S3E). Overall, these data show that the histone acetylation landscape becomes specified early in differentiation (Cao et al., 2006, 2010; Dilworth et al., 2004; Puri et al., 1997b).

To determine whether histone acetylation loss is directed by specific transcription factors, we performed promoter motif analysis. Remarkably, genes associated with decreased histone acetylation showed no significant motif enrichment (Figure 2G). The lack of enriched motifs diminishes the likelihood that a particular transcription or chromatin-modifying factor coordinates acetylation reduction. In contrast, promoter regions of genes associated with increased histone acetylation were highly enriched for MADS and E-Box motifs, which are bound by the MEF2 transcription factor family, and myogenic regulatory factors (MYF5, MYOD1, and MYOG), respectively (Bergstrom et al., 2002). This agrees with studies showing that MYOD1 associates with HATs p300 and CBP to activate transcription of myogenic targets (Polesskaya et al., 2001; Puri et al., 1997a). These data indicate that general reduction of histone acetylation occurs in conjunction with the gain of acetylation on myogenic genes. Given the lack of motif enrichment, we hypothesized that the histone acetylation reduction likely results from a broader change in cell state during differentiation.

Metabolic Alterations Characterize Distinct Myogenic Cell States

We postulated that changes in glucose metabolism could mediate the global reduction in histone acetylation during differentiation. Glucose-derived acetyl-CoA is known to be a source of histone acetylation, via PDH and ACLY (Evertts et al., 2013; Wellen et al., 2009) (Figure 3A). Labeling experiments have shown that histone acetylation turnover is highly dynamic (Zheng et al., 2013); therefore, we hypothesized that decreased availability of acetyl-CoA could result in reduced histone acetylation over a large range of genes and marks.

To identify changes in glucose metabolism, we compared the transcriptional profile of quiescent (freshly isolated), proliferating (2-day cultured), and early differentiating myoblasts. Analysis was paired with published microarray datasets of myoblast differentiation (GSE24811) (Soleimani et al., 2012). Activated and proliferating MuSCs exhibited a >2.5-fold upregulation of genes in anaerobic ATP generation and in lactate production (*Pgam1, Pgk1, Pkm, Ldha*) (Figure 3B; Table S2). In early differentiation, however, this expression pattern reversed. The expression of the rate-limiting enzyme *Pfkm* increased, while lower glycolysis genes decreased or stayed the same. In addition, expression of *Pdha1* increased, as did the mitochondrial pyruvate transporters *Mpc1* and *Mpc2*. These changes suggest reciprocal changes in glucose metabolism upon both MuSC activation and differentiation.

Early Myogenic Differentiation Is Marked by Metabolic Dysfunction and Glucose Reliance

We hypothesized that myoblasts increase glucose utilization for respiration during differentiation. We used Seahorse mitochondrial and glycolytic stress tests to assay the metabolic profile in growing (in GM) or early differentiating myoblasts (after 24-h DM). To assay the contribution of glucose to respiration, mitochondrial stress tests were performed in glucose (25 mM) and glucose-free media conditions (Figures 3C-3F), as well as the presence of pyruvate, 5 mM glucose, and combinations of glucose and pyruvate (Figures S4A-S4D) to control for the different concentrations in GM and DM.

We observed that myoblasts in GM did not require glucose for basal oxygen consumption or ATP-linked respiration (Figures 3C, 3D, and S4A-S4D). In glucose-free conditions, however, cells lacked spare capacity. This suggests that while myoblasts are capable of utilizing glucose for mitochondrial respiration under metabolic stress (i.e., FCCP), non-glucose sources fuel basal respiration. Compared to myoblasts in GM, however, differentiating myoblasts had a striking loss of respiratory capacity (Figures 3C, 3D, and S4A-S4D). Loss of mitochondrial function is consistent with the mitochondrial remodeling during reported during early differentiation (Kim et al., 2013; Sin et al., 2016). Early differentiating myoblasts had reduced Mitotracker Red staining, indicative of reduced membrane potential, and increased expression of FIS1, a marker of mitofission (Figures S4E and S4F). Glycolysis and glycolytic capacity were also reduced in differentiation (Figures 3E and 3F). Importantly, while glucose was not required for basal respiration or ATP production of proliferating myoblasts, both metrics were significantly reduced in early differentiating myoblasts without glucose. Spare capacity was almost completely absent in differentiating myoblasts, indicating that mitochondria are respiring at their maximum capacity.

PDH is a key regulator of mitochondrial utilization of glucose. Its activity is inhibited by pyruvate dehydrogenase kinases (PDKs) through reversible phosphorylation (Patel et al., 2014). Therefore, we sought to determine PDH activity at various stages of MuSC progression by assaying phosphorylation. Increased phosphorylated PDH (pPDH) was apparent in MuSCs on cultured single myofibers compared to freshly isolated fibers (Figures 3G and S4H). Using flow cytometry to measure pPDH and total PDH, we observed that pPDH ratio was increased ~5-fold in proliferating, cultured MuSCs compared to those freshly isolated (Figure 3H). Consistent with expression data and the increase in mitochondrial glucose utilization observed by Seahorse, early differentiating MYOG$^+$ progenitors had reduced pPDH (Figure 3I). We validated this finding in regenerating muscles *in vivo* by CyTOF, which confirmed an increase in pPDH/PDH ratio specifically in PAX7$^+$ MuSCs in injured tissue compared to uninjured, followed by a decrease in MYOG$^+$

differentiating progenitors (Figure 3J). Together, these data confirm our hypothesis that altered mitochondrial glucose utilization occurs upon MuSC activation and differentiation.

Glucose Metabolism Regulates Histone Acetylation State and Myogenic Differentiation

We used $^{13}C_6$-D-glucose isotopic labeling to directly measure glucose-derived histone acetylation in proliferation versus differentiation. In addition, we assayed the role of PDH by treating proliferating myoblasts with the PDK inhibitor dichloroacetate (DCA), which increases PDH activity (Stacpoole et al., 1998). Incorporation of labeled acetyl-CoA into histones was quantified by LC-MS/MS following 6 h of incubation with $^{13}C_6$-D-glucose media (GM, GM+DCA, or DM). Labeling was quantified as the fraction of labeled acetylation over total acetylation (labeled + unlabeled) for each mark (Evertts et al., 2013). In all, proliferating myoblasts were labeled in GM containing $^{13}C_6$-D-glucose (GM▶GM), or GM+DCA containing $^{13}C_6$-D-glucose (GM▶GM+DCA), or DM containing $^{13}C_6$-D-glucose (GM▶DM), and differentiating myoblasts were labeled in DM containing $^{13}C_6$-D-glucose (24-h DM▶DM) (Figure 4A).

All reliably detected histone acetylation marks contained >50% incorporation of ^{13}C following the 6-h pulse (Figure 4B), confirming the importance of glucose as a contributor to histone acetylation. Myoblasts labeled at the onset of differentiation (GM▶DM) showed a 2%–7% reduction in ^{13}C incorporation compared to those labeled in GM (GM▶GM). This reduction in ^{13}C incorporation was maintained 24 h after differentiation for H3 and H2A peptides, demonstrating that decreased flux to histone acetylation at the onset of differentiation is persistent.

DCA treatment reduced pPDH in cultured MuSCs, proliferating myoblasts, and early differentiating myoblasts (Figure S5A). Treatment of MuSCs or myoblasts with DCA resulted in no change in expression of *PDH* or *PDK* genes (Figure S5B; Table S2), or myogenic transcription factors (Figure S5C; Table S3). However, DCA treatment of myoblasts in GM increased ^{13}C-glucose-derived histone acetylation (~12.6%, 12.1%, 8.1%, 10.8% for H3K9|14, H3K18|23, H4K5|8|12|16, and H2A.1K5, respectively), indicating that histone acetylation is limited by PDH activity in proliferating myoblasts (Figure 4B). Antibody staining confirmed an overall increase in histone acetylation with DCA by 15%-116% for all marks assayed (Figure 4C). These results show that turnover of glucose-derived histone acetylation is dynamic and limited by PDH in proliferating myoblasts. During differentiation, decreased glucose-derived histone acetylation occurs in concordance with the decreased total histone acetylation. These findings indicate that regulation of glucose metabolism contributes to broad changes in histone acetylation.

Glucose-Derived Histone Acetylation Is a Key Modifier of Myogenic Differentiation

To establish whether glucose-derived histone acetylation regulates MuSC function and myogenic differentiation, we assessed the differentiation capacity of myoblasts following DCA treatment. DCA-treated MuSCs cultured on hydrogels for 7 days retained PAX7 expression and gave rise to fewer MYOG^{+} cells compared to untreated controls, suggesting maintenance of the stem cell state (Figures S5D and S5E). In accordance with the reduction in spontaneous differentiation, treatment of myoblasts with DCA in GM alone was sufficient to reduce the percentage of myoblasts expressing MYOG after 24 h in DM (Figures 4D and 4E). In striking contrast, treatment of myoblasts with DCA in DM alone had no effect on differentiation, suggesting that DCA cannot reverse or prevent MYOG expression following commitment. Finally, at late differentiation (day 4), persistent DCA treatment (GM and DM) significantly reduced the percent of nuclei in MyHC$^+$ cells (Figures S5F and S5G). These data show that increased PDH activity in myoblasts, which increases total histone acetylation, hinders the transition toward a committed myocyte.

We sought to determine whether reduced glucose-derived histone acetylation is sufficient to induce early differentiation in proliferating cells in GM. Knockdown of *Acly* was identified in a short hairpin RNA (shRNA) screen as a strong inducer of MYOG and MyHC in C2C12 cells in the presence of serum (Bracha et al., 2010). In agreement, we found that small interfering RNA (siRNA)-mediated knockdown of *Acly* (*siAcly*) in primary myoblasts, in GM conditions, reduced histone acetylation by 50% and resulted in an approximately 3-fold increase in the percentage of MYOG$^+$ cells (Figures 4F-4H). Notably, si*Acly* led to a gradient of reduced histone acetylation levels, with MYOG$^+$ cells appearing when acetylation levels were maximally reduced. Consistent with PDH upstream of ACLY, DCA treatment with *siAcly* did increase histone acetylation or prevent the appearance of MYOG$^+$ cells. Similar results were observed with siRNA-mediated knockdown of citrate synthase (*siCs*) (Figures 4I and 4J). Again, the phenotype of *siCs* is dominant over DCA treatment, in agreement with our hypothesis that DCA-induced histone acetylation depends on glucose metabolism. Treatment of proliferating myoblasts with FCCP, a mitochondrial uncoupler that stimulates oxidation of TCA substrates to meet increased energy demand, also reduced histone acetylation (Figure S5H). These data show that glucose-derived acetyl-CoA is critical for maintaining histone acetylation levels and that overall level of histone acetylation modulates commitment toward differentiation.

Mitochondrial Remodeling Restricts Histone Acetylation during Differentiation

A transient phase of mitofission and mitophagy occurs at the early stages of myogenic differentiation (Sin et al., 2016). We hypothesized that this could contribute to the decrease in histone acetylation. To assay the role of mitochondrial remodeling in histone acetylation, myoblasts were treated with Mdivi-1, a Drp1 inhibitor that prevents mitochondrial fission, in GM or DM (Cassidy-Stone et al., 2008). Mdivi-1 had no effect on histone acetylation or percentage of cells expressing MYOG in GM. However, Mdivi-1 treatment in DM increased histone acetylation and reduced MYOG$^+$ cells after 24 h differentiation (Figures 4K-4M). Intriguingly, histone acetylation in Mdivi-1-treated differentiating progenitors was increased compared to untreated myoblasts in GM. This is likely due to the increased PDH activity observed during early differentiation (Figures 3I and 3J). These findings suggest that mitochondrial remodeling during early differentiation limits glucose-derived histone acetylation, despite increased PDH activity. Overall, these findings confirm that glucose metabolism is a critical determinant of histone acetylation and differentiation capacity, and loss of histone acetylation is mediated by mitochondrial remodeling during early differentiation.

Increased Glucose-Derived Acetylation Reinforces the Epigenetic Landscape of Proliferating Myoblasts

To address how glucose metabolism modifies the epigenetic landscape, we assayed H3K9|14ac by ChIP-sequencing and chromatin accessibility by ATAC-seq following 24-h DCA treatment. On average, DCA-treated cells had significantly increased histone acetylation near TSSs across the genome (Figures 5A-5C), consistent with the observed increase in overall histone acetylation. Increased histone acetylation was primarily seen at promoter regions that already showed detectable H3K|14ac (Figures 5B and 5C). Promoters with low signal in control samples, such as at myogenic differentiation genes in GM, had no change or reduced histone acetylation upon DCA treatment. This is consistent with increased substrate levels for existing HAT activity, which results in an overall increase in existing histone acetylation sites, rather than *de novo* deposition of acetylation marks by an increased activity of a specific transcription factor.

This hypothesis was confirmed by Gene Ontology (GO) analysis of genes associated with histone acetylation changes. Promoter regions (± <2 kb from TSS) with >2-fold increase in histone acetylation following DCA were annotated to 5,136 genes. A comparison with myogenic differentiation showed that about one-half of these genes (2,787) lost histone acetylation on one or more marks (H3K9, H4K12, H4K16, and H3K27) in myotubes (Figure 5D). Genes that both lost histone acetylation in myotubes and gained histone acetylation with DCA were enriched for chromatin regulation, cell cycle, gene expression regulation, and muscle cell proliferation. There was little overlap (283 genes) between genes that gained histone acetylation in myotubes with those that gained histone acetylation with DCA. This is in contrast to the genes that gained histone acetylation during differentiation but did not respond to DCA, which are enriched for muscle-specific GO terms (Figure 5D).

In concordance with H3K9|14ac accumulation at the enhancers or promoters of poised or actively transcribed genes, we found increased expression in genes associated with increased histone acetylation at proximal promoters (± <2 kb from TSS), and to a lesser extent, distal enhancers (−100 kb) (Figure 5E). Overall, these data support that glucose metabolism is rate limiting for histone acetylation, and that PDH activity acts as a rheostat for acetylation of established enhancers and promoters.

We used ATAC-seq to assess chromatin accessibility changes upon DCA treatment. ATAC-seq signal correlates with accessible chromatin and is enriched in enhancers and promoter elements (Buenrostro et al., 2013). Consistent with the hypothesis that PDH-mediated histone acetylation occurs primarily on already acetylated, open chromatin, we observed increased H3K9|14ac ChIP signal at peaks closely associated with ATAC-seq peaks, which was also correlated with the number of associated ATAC-seq peaks (Figures 5F-5H). Furthermore, ATAC-seq signal was increased for a subset of peaks in DCA-treated (Figure 5I) and was associated with an increase in expression of genes with ATAC-seq peaks in their proximal promoters (± <2 kb from TSS) (Figure 5J). Motif analysis of regions that gained accessibility with DCA showed enrichment for consensus sequences of several transcription factors, in particular the core promoter element CCAAT (Figure 5K). This motif is bound by CCAAT-enhancer binding proteins (C/EBPs), which are known to recruit transcription factors as well as chromatin modifiers (Mink et al., 1997; Nerlov, 2007). C/EBPβ has been shown have high expression in MuSCs and declines during early differentiation (Marchildon et al., 2012). Overexpression of C/EBPβ has been shown to inhibit myogenic differentiation, while loss of C/EBPβ leads to precocious differentiation (Lala-Tabbert et al., 2016). These data highlight the role of C/EBPs in preserving the stem/progenitor cell chromatin state. Moreover, they support our hypothesis that PDH activity is a rate-limiting step in histone acetylation and dictates the accessibility around myoblast genes. Accordingly, increasing PDH activity in proliferating myoblasts reinforces histone acetylation and chromatin accessible regions that are already present, delaying progression toward differentiation.

Dysregulation of PDH *In Vivo* Results in Aberrant Histone Acetylation and Reduced Skeletal Muscle Regeneration

To assess the role of PDH in muscle regeneration we used the *Pdk2/Pdk4* double-knockout (dKO) mouse model, which has increased acetyl-CoA due to constitutively active PDH (Jeoung et al., 2012; Rahimi et al., 2014). We confirmed the absence of *Pdk2* and *Pdk4*, and the lack of compensation in proliferating MuSCs by expression of other PDK isoforms (*Pdk1* and *Pdk3*) (Figure 6A), as well as the lack of PDH phosphorylation during regeneration (Figure 6B).

Regeneration and MuSC dynamics were assessed in uninjured TA muscle (D0) and 6 or 12 days (D6 and D12, respectively) postinjury by notexin injection. At D0, no difference in the number of PAX7$^+$ MuSCs was observed between dKO and wild-type (WT) (Figure 6C). At D6, both genotypes exhibited a similar increase in numbers of PAX7$^+$ MuSCs. No differences in Ki67$^+$ MuSCs, or Cleaved Caspase-3 were observed at D6, consistent with no differences in proliferation or cell death (Figures S5A and S5B). However, at D12, dKO animals exhibited a ~50% increase in the number of MuSCs (Figures 6C and 6D), suggesting that constitutive PDH activity could be enforcing self-renewal over differentiation, as we observed *in vitro* (Figures 4D and 4E). Flow cytometry of H3K18 and H4K16 acetylation showed that MuSCs in dKO animals had no difference in histone acetylation prior to injury (Figure 6E) but accumulated increased histone acetylation following injury (D6) (Figure 6F). Furthermore, we observed a decreased proportion of MYOG$^+$ myogenic progenitors in dKO mice at D6 (Figures 6G and 6H). Underscoring a differentiation defect, dKO muscles had reduced cross-sectional area at D12 postinjury (Figures 6I and 6J), despite increased numbers of MuSCs at this time point. Together, these results suggest that the MuSCs of *Pdk2/4* dKO mice develop normally but are biased toward self-renewal and reduced differentiation capacity due to an aberrant accumulation of histone acetylation.

To confirm the differentiation deficits we observed in dKO mice are MuSC-intrinsic, we assayed engraftment of WT or dKO MuSCs transplanted in Pdk2/4$^{+/+}$ recipient muscle using bioluminescence imaging (BLI) (Sacco et al., 2008). Isolated MuSCs were labeled with a luciferase-expressing lentivirus and transplanted into irradiated hind-limb muscles of immunodeficient NOD *scid* gamma (NSG) animals (Figure 6K). 28 days after transplantation, dKO MuSCs showed reduced bioluminescence signal, indicative of reduced differentiation and contribution of donor dKO MuSCs to myofibers (Figures 6J and 6K). This suggests that dKO MuSCs have a cell-autonomous reduction in differentiation capacity, which is attributable to the irreversible dysregulation of PDH activity. These data substantiate our findings that glucose metabolism regulates histone acetylation during proliferation and modulates myogenic differentiation both *in vitro* and *in vivo*.

DISCUSSION

In this study, we elucidate the role of glucose metabolism as an epigenetic regulator of proliferating MuSCs, and a modulator of differentiation capacity. We characterize distinct, interrelated metabolic and histone acetylation states of MuSCs in uninjured and injured muscle tissues, as well as in differentiating progenitors. In particular, we identify PDH activity as a pivotal regulator of glucose-derived histone acetylation during MuSC expansion, which dictates the transition toward differentiation.

MuSCs in uninjured tissues exist in a quiescent cell state with low metabolic demand and few mitochondria (Muir et al., 1965; Pala et al., 2018). Nevertheless, quiescent MuSCs show signatures of glucose and fatty acid oxidation and low lactate-producing glycolysis (Ryall et al., 2015). This results in low levels of histone acetylation, due to utilization of acetyl-CoA, as well as high levels of NAD^+ leading to active histone deacetylation by SIRT1 (Ryall et al., 2015). Upon activation, MuSCs undergo mitochondrial biogenesis, and increase lactate-producing glycolysis (Pala et al., 2018; Rodgers et al., 2014). This is marked by increased expression of lower-glycolysis genes (Figure 3B), diminished requirement for glucose to support respiration (Figures 3C and 3D), and increased PDH phosphorylation (Figures 3G, 3H, and 3J). In addition to the resulting decreased SIRT1 deacetylase activity (Ryall et al., 2015), these metabolic changes result in overall increased histone acetylation (Figure 4B). In this state, PDH activity is rate limiting for glucose-derived histone acetylation (Figures 4B, 4C, and 5A-5D).

At the onset of differentiation, metabolic remodeling drives reduction in histone acetylation (Figures 1C-1G and 2A-2D). Mitophagy and mitochondrial fission decrease capacity of mitochondria, which in turn have increased reliance on glucose (Figures 3C-3F) (Sin et al., 2016). These metabolic changes reduce the contribution of glucose to histone acetylation (Figure 4B), resulting a global reduction in histone acetylation across multiple marks during differentiation *in vivo* (Figure 1) and *in vitro*. Conversely, forced reduction of glucose-derived histone acetylation results in precocious induction of differentiation (Figure 4), which has been shown to be dependent on histone acetylation (Bracha et al., 2010). We find that histone acetylation is lost across the genome during differentiation; however, genes associated with differentiation such as MYOG increase histone acetylation. Thus, metabolic histone acetylation regulation acts in conjunction with regulation by histone modifiers and transcription factors.

It is important to note that metabolic modulation of histone acetylation is not equivalent to regulation by transcription factors, HDACs, or HATs. Our site-specific analyses suggest that, with substrate limitation, the availability of acetyl-CoA modulates histone acetylation at sites already targeted by HAT and HDACs. Sites not targeted by HATs, have low acetylation turnover, or are maintained at a low acetylation state by HDACs, are less susceptible to substrate limitations. Conversely, HDAC inhibitors (HDACis) will increase histone acetylation at genes targeted by HDACs. Even though both HDACi and DCA treatment result in increased histone acetylation, the affected sites are different. During proliferation, MYOD1 has been shown to act with HDACs to deacetylate myogenic differentiation genes (Lu et al., 2000; Puri et al., 2001). Thus, when proliferating myoblasts are treated with HDACis, histone acetylation increases on myogenic differentiation genes to promote differentiation (lezzi et al., 2002, 2004). Treatment with DCA, on the other hand, does *not* affect differentiation genes (Figures 5A-5D). Instead, DCA treatment reinforces the overall epigenetic landscape of proliferating progenitors and stabilizes expression of stem cell genes (Figures 5D and 5E).

During differentiation, loss of histone acetylation around stem cell genes facilitates a change in cell identity, transitioning toward *de novo* acetylation around muscle-specific genes. Intriguingly, while loss of glucose-derived histone acetylation triggers differentiation, knockdown of the HAT CBP and p300 inhibits differentiation (Polesskaya et al., 2001; Puri et al., 1997a). This is because CBP/p300, also directed by MYOD1, is required to acetylate and activate transcription of myogenic differentiation genes. As such, HDACi treatment at the onset of differentiation by serum removal abolishes differentiation. Further supporting this idea, *Acly* knockdown in proliferation conditions induces differentiation (Bracha et al., 2010), while knockdown in differentiation conditions reduces muscle gene expression and myotube hypertrophy (Das et al., 2017). Recent insights from single-cell ATAC-seq agree with this idea (Pliner et al., 2018), wherein differentiation begins with closing of a large number of sites, followed by a subset of specific sites that gain acetylation and accessibility (of which 70% are bound by MYOD1) (Cao et al., 2010).

We thus propose two complimentary mechanisms of histone acetylation changes that coordinate during myogenic differentiation: (1) the active deacetylation and acetylation of myogenic genes by the interaction of MYOD1 with HDACs and HATs, and (2) regulation by shifts in metabolic state described here. Global histone acetylation loss, mediated by altered glucose metabolism, has also been observed in differentiating embryonic stem cells (Moussaieff et al., 2015), but has not been previously described in the context of tissue-specific stem cells in regeneration. Our results raise the possibility that the metabolic regulation of histone acetylation on non-lineage specific genes may be a hallmark of tissue-specific stem cell specification.

STAR★METHODS

LEAD CONTACT AND MATERIALS AVAILABILITY

Further information and requests for resources and reagents should be directed to and will be fulfilled by the Lead Contact, Helen Blau (hblau@stanford.edu).

EXPERIMENTAL MODEL AND SUBJECT DETAILS

The Stanford University Administrative Panel on Laboratory Animal Care (APLAC) approved all animal protocols. We performed all experiments in compliance with the institutional guidelines of Stanford University. C57BL/6J mice were purchased from Jackson Laboratories and used at 8-16wk. PDK2/PDK4 double knockout mice were provided by a generous gift from Robert Harris (Indiana University). All experiments were conducted using age and gender-matched controls, and littermates randomly assigned to experimental groups. Both male and female animals were used.

METHOD DETAILS

Notexin-induced muscle injury—For muscle injury, we performed an intramuscular injection of 10 μL of notexin (10 μg ml–1; Latoxan) into the *tibialis anterior* or *gastrocnemius* muscle. For uninjured controls, we collected muscle from completely uninjured mice. Muscles were collected in uninjured mice, as well as day 6 after injury for flow cytometry and CyTOF analyses, and day 6 and day 12 for immunohistochemistry analysis.

Florescence activated cell sorting—Muscle stem cells were isolated using a modified version of the protocol previously described (Sacco et al., 2008). In brief, hind-limb muscles were isolated and dissociated using the gentleMACS Octo Dissociator with a modified manufacturer protocol (Miltenyi Biotech). Dissociated muscle was digested with 0.2% collagenase (Roche) for 60min, followed by collagenase/dispase (0.04 U ml–1; Roche) digestion for 30 minutes. MuSCs were liberated by syringe dissociation with an 18G needle. Cells were incubated with biotinylated antibodies against CD11b (1:800), CD45 (1:500), Sca1 (1:200) and CD31 (1:200), followed by incubation with streptavidin magnetic beads (Miltenyi Biotech), streptavidin-APC-Cy7, integrin-α_7-PE (1:500) and CD34-eFluor660 (1:67). After magnetic depletion on a selection column (Miltenyi) for biotin-positive cells, (CD45$^-$CD11b$^-$CD31$^-$Sca1$^-$) CD34$^+$integrin-$\alpha_7{}^+$ MuSCs were double-sorted by flow cytometry to > 95% purity (DIVA-Van, Becton Dickinson).

Flow Cytometric Analysis—For analytical flow cytometry, cells or whole-muscle mixtures were fixed in 1.6% paraformaldehyde for 10min at room temperature (myoblasts, whole tissue digests) or on ice (MuSCs), and permeabilized on ice with ice-cold MeOH. Cells were used after 10 minutes on ice, or after storage in −20 for up to two weeks. After washing with PBS, cells were blocked using sterile filtered 0.5% bovine serum albumin (BSA) in PBS. Cells were incubated with primary antibody for 1hr at room temperature at a density of 1×10^6 cells/mL, washed 2X in PBS then stained in secondary for 20 minutes. Three washes were done before resuspension in DAPI/PBS and analyzed by LSR.II.UV. For myogenic staining, antibodies used were mouse anti-Myogenin, rabbit anti-Myogenin and mouse anti-Pax7. For acetylation analysis by flow, rabbit anti-H4K16ac, rabbit anti-H3K18ac, mouse anti-H3K9ac, rabbit antiacetyl-Histone H3, and total histone H3 were used. DNA content was measured by DAPI staining or 7-AAD. Data were collected using the LSR-II.UV (Becton Dickinson) and analyzed by FlowJo.

Single Cell Mass Cytometry (CyTOF)—9-12wk old wild-type C57/Bl6 were injured 6 days before collection by notexin injection. Injured and uninjured mice were injected with Idu at 8hr and 30minutes before sample collection to label dividing cells. Whole muscle single-cell suspensions of uninjured and notexin-injured C57/BL6 mice were obtained as described in **Fluorescence Activated Cell Sorting.** Single-cell suspensions were passed twice through a 40uM filter to remove debris, and fixed using 1.6% paraformaldehyde. Cells were first labeled with metal-conjugated surface antibodies for 1hr at room temperature, and then permeabilized for 10 minutes on ice with 90% methanol. Permeabilized cells were labeled with metal-conjugated intracellular markers, washed and kept overnight at 4C with iridium DNA intercalator. All antibodies were conjugated to isotopically pure lanthanide metal using the MaxPAR antibody conjugation kit according to the manufacturer's recommended protocol. Labeled antibodies were stored at 4-C in PBS-based Antibody Stabilizer (Candor Bioscience). Samples were run on the CyTOF mass cytometer (DVS Sciences). Muscle antibody panel developed by Ermelinda Porpiglia and histone acetylation antibody panel developed by Sean Bendall and Michael Angelo. See Table S1 for antibodies and metal conjugation.

RNA Sequencing—α7-integrin$^+$CD34$^+$ muscle stem cells were isolated as described above and processed either fresh or after 48hr of culture on 12kPa hydrogels. RNA was isolated using QIAGEN RNAEasy Micro kit from 5-10,000 cells, and cDNA generated and amplified using NuGEN Ovation RNA-Seq System v2 kit. Libraries were constructed from cDNA with the TruSEQ RNA Library Preparation Kit v2 (Illumina), and sequenced to 30-40×10^6 1×75bp reads per sample on a HiSEQ 2500.

Chromatin Immunoprecipitation—~1×10^7 primary myoblasts at 50%–75% confluence were cross-linked in 1% formadehyde for 15 min, with constant agitation, and quenched with 150mM glycine for 5 min. Micrococcal nuclease (New England Biolabs, Inc.) was used to fragment chromatin to a range of 200-400 bp. Chromatin was incubated with H3ac antibody overnight at 4°C with constant agitation. Protein A Dynabeads was incubated with antibody-protein complexes for 2 hr at 4°C with constant agitation. After de-crosslinking, DNA was isolated using a MinElute column (QIAGEN). See Quantitative Real Time PCR for quantification of target genes.

ATAC-Seq—50,000 primary myoblasts were prepared according to Buenrostro et al. (2013) using the Nextera DNA Library Preparation Kit. In brief, cells were washed with PBS and lifted using 0.125% trypsin for 5 mins at 37C then pelleted. The pellet were resuspended in ice cold lysis buffer (10 mM Tris-HCl, pH 7.4, 10 mM NaCl, 3 mM MgCl2, 0.1% IGEPAL CA-630), pelleted and resuspended in Tn5 transposase according to manufacturer's instructions. The reaction was incubated for 30 minutes at 37C on a shaker. Transposed DNA was isolated using the QIAGEN MinElute Reaction Cleanup Kit. Libraries were amplified for a total of 8-10 PCR cycles (adjusted to 25% of saturation by qPCR), and sequenced in parallel to 97 ×10^6 and 91×10^6 2×37bp reads for PBS and DCA-treated samples, respectively, on Illumina NextSeq High Output. After removal of mitochondrial DNA reads, 90.6×10^6 and 92.3×10^6 paired end reads with mapQ scores of 10+ were used in downstream analysis for PBS and DCA samples, respectively.

Immunofluorescence and histology—Muscle tissues were prepared for histology as described previously described (Sacco et al., 2008). For immunofluorescence, anti-Pax7, anti-laminin, anti-phosphoPDH (Ser293), anti-PDH E1 alpha subunit, anti-Ki67, anti-Cleaved Caspase-3 and mouse anti-Myosin Heavy Chain antibodies were used. All AlexaFluor secondary antibodies were used (1:500), and nuclei counterstained with DAPI.

Image Analysis—*In vitro* differentiation was quantified by immunocytochemical analysis. Differentiated cells fixed in-well were analyzed by confocal microscopy. 4-5, 20X fields of view were acquired. Blinded samples were analyzed by MetaMorph© software to determine MyHC positivity. *In vivo* immunohistochemical images quantified by 8-12, serial sections spanning approximately 2mm length of tissue. For quantification of Pax7$^+$, Ki67$^+$ and Cleaved Caspase-3$^+$ cells, 3-5 non-overlapping fields of view were captured per section at 20X. Blinded samples were analyzed by MetaMorph© software to determine Pax7 or Ki67 positivity. Cross-sectional area was determined using the Baxter Algorithms for Myofiber Analysis.

Histone Extraction and Derivatization—Histones were extracted and derivatized similar to previously described methods (Lin and Garcia, 2012). Frozen cell pellets were resuspended in nuclear isolation buffer (NIB; 15 mM Tris HCl pH 7.5, 15 mM NaCl, 60 mM KCl, 5 mM $MgCl_2$, 1 mM $CaCl_2$, 250 mM sucrose supplemented with 1 mM DTT, 10 mM sodium butyrate, 500 µM AEBSF, and 5 nM microcystin) containing 0.2% NP-40 alternative and incubated on ice for 10 mins. Nuclei were pelleted by centrifugation at 500 × g for 5 mins at 4°C and washed twice in detergent-free NIB. Histones were extracted from nuclei with 0.4N H_2SO_4 for approximately 4 hr at 4°C with rotation. Histone extracts were cleared by centrifugation at 3400 × g for 5 mins at 4°C and the supernatants were precipitated by adding 1 volume of 100% trichloroacetic acid to 3 volumes of sample and incubating overnight at 4°C. Precipitated histones were pelleted at 3400 × g for 5 mins at 4°C and washed sequentially with 0.1% HCl in acetone and then acetone alone. After air drying, histone pellets were resuspended in 100 mM ammonium bicarbonate. Approximately 8-10 µg of protein were subjected to derivatization, in which free lysine residues were proprionylated by adding 1 volume of 25% proprionic anhydride/75% 2-propanol to 2 volumes of sample and incubating for 15 mins at 37°C. Additional ammonium bicarbonate salt was added at the beginning of the reaction to prevent the pH from becoming too acidic. Samples were dried in a speed vac and then proprionylated a second time. Proprionylated histones were resuspended in 100 mM ammonium bicarbonate and digested with trypsin (1/20 ratio by mass) overnight at room temperature. Digested peptides were proprionylated twice more as above and then desalted with C18 stage tips prior to mass spectrometry analysis.

Mass Spectrometry—Derivatized histone peptides were loaded into an Easy nLC 1000 (Thermo) liquid chromatography system fitted with 75 µm i.d. × 20 cm fused silica columns (Polymicro Tech), pulled and packed in house with ReproSil-Pur 120 C18-AQ (3 µm, Dr. Maisch GmbH), in line with an Orbitrap Elite or Velos (Thermo). Peptides were separated using a gradient of 2%–30% buffer B (0.1% formic acid in acetonitrile) in buffer A (0.1% formic acid in water) over 35 mins and 30%–98% over 20 mins. Full scan mass spectra from 290-1400 m/z were acquired at a resolution of 60,000 with automatic gain control set at 1E6. Tandem mass spectra were acquired by CID fragmentation at a normalized collision energy of 35 and maximum injection time of 150 ms with automatic gain control set at 5E4. MS data were searched and quantified with EpiProfile

Oxygen Consumption and Extracellular Acidification analysis—Primary myoblasts were plated at a 1×10^4 cells/well of a collagen coated 96-well Seahorse cell culture plate and grown for 48hrs ± DCA in standard myoblasts growth media (+1g/L glucose, 1mM Pyruvate). As a negative control, one row of the culture plate was left without only media and no cells as a negative control. One day before measurements, a Seahorse sensor cartridge was prepared according to manufacturer's instructions, with overnight incubation at 37°C in a CO_2-free incubator. On the day of measurements, cells were washed twice and switched to un-buffered DMEM + Glutamine (Agilent) supplemented with 15% dialyzed fetal bovine serum (FBS) adjusted to pH of 7.4. For each condition (±DCA, pH 7.4), one row was supplemented with 1g/L glucose and 1mM pyruvate to assay respiration with available carbohydrate substrates, and one row left un-supplemented to assay non-carbohydrate respiration and lactate production. Cells were equilibrated at 37°C in a CO_2-free incubator for one hour. Inhibitors (Oligomycin, Carbonyl cyanide-*4*-(trifluoromethoxy)phenylhydrazone (FCCP), and Rotenone/Antimycin) were added each at a final concentration of 1 μM after injection to the appropriate port of the sensor cartridge. The cell culture plate and sensor cartridge were run on the Seahorse XF-96, and data analyzed by Excel.

Quantitative Real Time PCR—Total RNA was isolated using the RNAeasy Mini kit (QIAGEN). The RNA concentration was determined with a spectrophotometer, and up to 1ug was used to prepare cDNA (Ready-To-Go, T-Primed First-Strand Kit, Amersham Bioscience 27-9263-01). Inventoried TaqMan FAM probes (Applied Biosystems) were used for the relative quantification of the mRNA levels of Pdha1, Pdk1, Pdk2, Pdk3, Pdk4, Pax7 and Acly. For ChIP-qPCR, SYBR green was used with primers designed to span 80-100bp around H3ac ChIP-Seq peaks identified in C2C12 data (ENCODE/Caltech, GEO accession: GSE36023). For full primer sequences see Table S2.

Lentiviral Infection—Sorted MuSCs were plated on collagen coated 24-well plates for 24hrs and infected with a luc-IRES-GFP lentivirus for 24hrs. Efficiency of transduction was evaluated by GFP staining of excess cells after 6 days in culture.

Bioluminescent Imaging—Five hundred MuSCs transduced with luc-IRES-GFP virus for 24 hours were injected in a volume of 10uL into the *tibialis anterior* muscle of NSG recipient animals. Recipient animals were irradiated with 18Gy 48hrs prior to transplantation. Bioluminscent imaging was performed using a XENOGEN-200 system as previously described (Sacco et al., 2008). Briefly, we anesthetized mice using isoflurane and administered 100 μL D-luciferin (0.1 mmol kg^{-1}, reconstituted in PBS; Caliper LifeSciences) by intraperitoneal injection. We analyzed BLI using a 60 s exposure acquired at 12 min after luciferin injection. Digital images were recorded and analyzed using Living Image software (Caliper LifeSciences). We analyzed images with a consistent region-of-interest (ROI) placed over each hindlimb to calculate a bioluminescence signal. We used a bioluminescence signal value of 70,000 photons per second to define an engraftment threshold.

Hydrogel fabrication—We fabricated polyethylene glycol (PEG) hydrogels from PEG precursors, synthesized as described previously (Gilbert et al., 2010). Briefly, we formed hydrogels by mixing 10% (wt/vol) solutions of PEG-sulfhydryl (4-arm 10-kDa PEG-SH) and PEG-vinylsulfone (8-arm 10-kDa PEG-VS) precursor polymers diluted in water or triethanolamine, respectively. We functionalized hydrogel surfaces through covalent cross-linking reaction with PBS-dialyzed laminin protein (Roche). We fabricated soft 12-kPa (Young's modulus) stiffness hydrogels to 1-mm thickness (Gilbert et al., 2010). We fabricated hydrogels to a 1-μm thickness directly onto tissue culture plastic dishes to achieve a rigid 1 × 106-kPa stiffness, as hydrogels of ≤ 1-μm thickness allow cells to sense the underlying substrate mechanical properties, resulting in an effective rigidity equivalent to tissue culture plastic (Engler et al., 2006; Gilbert et al., 2010), while providing equivalent material surface chemistry as thicker soft gels. This non-swelling gel chemistry results in equivalent laminin protein concentrations (estimated to be 7.5 ng cm–2 in ref. 32) on both soft and rigid hydrogels. We cut and adhered all hydrogels to cover the surface area (2.0 cm2) of 24-well culture plates.

Data Reporting—Sample size was determined based on practical and experimental consideration, with no statistical methods used to predetermine sample size. For florescence data, investigators were blinded to allocation for image acquisition and analyses.

QUANTIFICATION AND STATISTICAL ANALYSIS

Statistical Analysis—All values expressed as mean ± s.e.m. Differences with *p* value < 0.05 were considered significant (*p < 0.05, **p < 0.01, ***p < 0.001). Comparisons between two groups were performed using Student's t test (two-tailed, paired and unpaired where indicated). For multiple comparisons, 1-Way or Repeeated Measures ANOVA with Tukey's Test or 2-way ANOVA with Bonferonni correction were conducted.

Sequencing Analysis—RNA, ChIP and ATAC-seq data were aligned against the *Mus musculus* mm10 genome using STAR (Dobin et al., 2013) or BWA (Li and Durbin, 2009). (for RNA and ChIP/ATAC, respectively). RSEM (Li and Dewey, 2011) was used for calling transcripts and calculating transcripts per million (TPM) values, as well as total counts. MACS2 (Zhang et al., 2008) was used for peak calling for ChIP and ATAC-seq data. ATAC-seq peaks were further refined as ± 75bp regions of peak summits identified by MACS2. Common satellite repeat regions were removed against the UCSC Repeatmasker track. A counts matrix containing the number of counts for each gene/peak and each sample was obtained. This matrix was analyzed by DESeq to calculate statistical analysis of significance (Anders and Huber, 2010) of genes between samples. Gene annotation for ChIP and ATAC peaks were performed using GREAT using regions ± 2 kb proximal and 100kb distal from the transcription start site (TSS) as well as curated regulatory domains. Motif analyses were performed using HOMER using either −300bp to +50bp proximal promoter regions of genes of interest or within peaks identified by ChIP or ATAC-seq.

DATA AND CODE AVAILABILITY

Sequencing (RNA, ChIP, ATAC) data have been submitted in MIME-compliant format to GEO, accession number super series GSE129280. Data available upon publication.

Supplementary Material

Refer to Web version on PubMed Central for supplementary material.

ACKNOWLEDGMENTS

Cell sorting and flow cytometry analysis for this project was done on instruments in the Stanford Shared FACS Facility. Data (or sorting) were collected (performed) on an instrument in the Shared FACS Facility obtained using NIH S10 Shared Instrument Grant S10RR027431-01. We thank Garry Nolan for use of his CyTOF mass cytometer. Robert M. Angelo and Sean Bendall kindly provided conjugated histone acetylation antibodies for our CyTOF panel. This study was supported by NIH grants R01 NS089533 and AG020961, California Institute for Regenerative Medicine grant RB5-07469 (awarded to H.M.B.), and the Baxter Foundation. N.Y. was supported by the National Science Foundation Graduate Research Fellowship Program (GRFP) (1309047). Y.X.W. was supported by the Canadian Institutes of Health Research. T.M. was supported by NIH Postdoctoral Individual National Research Service Award F32 GM112425-02. E.P. was supported by a BD Biosciences Stem Cell grant.

REFERENCES

Anders S, and Huber W (2010). Differential expression analysis for sequence count data. Genome Biol. 11, R106. [PubMed: 20979621]

Asp P, Blum R, Vethantham V, Parisi F, Micsinai M, Cheng J, Bowman C, Kluger Y, and Dynlacht BD (2011). Genome-wide remodeling of the epigenetic landscape during myogenic differentiation. Proc. Natl. Acad. Sci. USA 108, E149–E158. [PubMed: 21551099]

Bendall SC, Simonds EF, Qiu P, Amir AD, Krutzik PO, Finck R, Bruggner RV, Melamed R, Trejo A, Ornatsky OI, et al. (2011). Single-cell mass cytometry of differential immune and drug responses across a human hematopoietic continuum. Science 332, 687–696. [PubMed: 21551058]

Bergstrom DA, Penn BH, Strand A, Perry RLS, Rudnicki MA, and Tapscott SJ (2002). Promoter-specific regulation of MyoD binding and signal transduction cooperate to pattern gene expression. Mol. Cell 9, 587–600. [PubMed: 11931766]

Blum R, and Dynlacht BD (2013). The role of MyoD1 and histone modifications in the activation of muscle enhancers. Epigenetics 8, 778–784. [PubMed: 23880568]

Blum R, Vethantham V, Bowman C, Rudnicki M, and Dynlacht BD (2012). Genome-wide identification of enhancers in skeletal muscle: the role of MyoD1. Genes Dev 26, 2763–2779. [PubMed: 23249738]

Bracha AL, Ramanathan A, Huang S, Ingber DE, and Schreiber SL (2010). Carbon metabolism-mediated myogenic differentiation. Nat. Chem. Biol 6, 202–204. [PubMed: 20081855]

Brack AS, Bildsoe H, and Hughes SM (2005). Evidence that satellite cell decrement contributes to preferential decline in nuclear number from large fibres during murine age-related muscle atrophy. J. Cell Sci 118, 4813–4821. [PubMed: 16219688]

Buenrostro JD, Giresi PG, Zaba LC, Chang HY, and Greenleaf WJ (2013). Transposition of native chromatin for fast and sensitive epigenomic profiling of open chromatin, DNA-binding proteins and nucleosome position. Nat. Methods 10, 1213–1218. [PubMed: 24097267]

Cao Y, Kumar RM, Penn BH, Berkes CA, Kooperberg C, Boyer LA, Young RA, and Tapscott SJ (2006). Global and gene-specific analyses show distinct roles for Myod and Myog at a common set of promoters. EMBO J. 25, 502–511. [PubMed: 16437161]

Cao Y, Yao Z, Sarkar D, Lawrence M, Sanchez GJ, Parker MH, Mac-Quarrie KL, Davison J, Morgan MT, Ruzzo WL, et al. (2010). Genome-wide MyoD binding in skeletal muscle cells: a potential for broad cellular re-programming. Dev. Cell 18, 662–674. [PubMed: 20412780]

Cassidy-Stone A, Chipuk JE, Ingerman E, Song C, Yoo C, Kuwana T, Kurth MJ, Shaw JT, Hinshaw JE, Green DR, and Nunnari J (2008). Chemical inhibition of the mitochondrial division dynamin reveals its role in Bax/Bak-dependent mitochondrial outer membrane permeabilization. Dev. Cell 14, 193–204. [PubMed: 18267088]

Cerletti M, Jang YC, Finley LWS, Haigis MC, and Wagers AJ (2012). Short-term calorie restriction enhances skeletal muscle stem cell function. Cell Stem Cell 10, 515–519. [PubMed: 22560075]

Choudhary C, Weinert BT, Nishida Y, Verdin E, and Mann M (2014). The growing landscape of lysine acetylation links metabolism and cell signalling. Nat. Rev. Mol. Cell Biol 15, 536–550. [PubMed: 25053359]

Collins CA, Olsen I, Zammit PS, Heslop L, Petrie A, Partridge TA, and Morgan JE (2005). Stem cell function, self-renewal, and behavioral heterogeneity of cells from the adult muscle satellite cell niche. Cell 122, 289–301. [PubMed: 16051152]

Cooper RN, Tajbakhsh S, Mouly V, Cossu G, Buckingham M, and Butler-Browne GS (1999). In vivo satellite cell activation via Myf5 and MyoD in regenerating mouse skeletal muscle. J. Cell Sci 112, 2895–2901. [PubMed: 10444384]

Das S, Morvan F, Morozzi G, Jourde B, Minetti GC, Kahle P, Rivet H, Brebbia P, Toussaint G, Glass DJ, and Fornaro M (2017). ATP citrate lyase regulates myofiber differentiation and increases regeneration by altering histone acetylation. Cell Rep. 21, 3003–3011. [PubMed: 29241530]

Dilworth FJ, Seaver KJ, Fishburn AL, Htet SL, and Tapscott SJ (2004). In vitro transcription system delineates the distinct roles of the coactivators pCAF and p300 during MyoD/E47-dependent transactivation. Proc. Natl. Acad. Sci. USA 101, 11593–11598. [PubMed: 15289617]

Dobin A, Davis CA, Schlesinger F, Drenkow J, Zaleski C, Jha S, Batut P, Chaisson M, and Gingeras TR (2013). STAR: ultrafast universal RNA-seq aligner. Bioinformatics 29, 15–21. [PubMed: 23104886]

Engler AJ, Sen S, Sweeney HL, and Discher DE (2006). Matrix elasticity directs stem cell lineage specification. Cell 126, 677–689. [PubMed: 16923388]

Evertts AG, Zee BM, Dimaggio PA, Gonzales-Cope M, Coller HA, and Garcia BA (2013). Quantitative dynamics of the link between cellular metabolism and histone acetylation. J. Biol. Chem 288, 12142–12151. [PubMed: 23482559]

Feller C, Forné I, Imhof A, and Becker PB (2015). Global and specific responses of the histone acetylome to systematic perturbation. Mol. Cell 57, 559–571. [PubMed: 25578876]

Francetic T, Le May M, Hamed M, Mach H, Meyers D, Cole PA, Chen J, and Li Q (2012). Regulation of *Myf5* early enhancer by histone acetyltransferase p300 during stem cell differentiation. Mol. Biol. (N.Y.) 1, 5019. [PubMed: 25382872]

Fry CS, Lee JD, Mula J, Kirby TJ, Jackson JR, Liu F, Yang L, Mendias CL, Dupont-Versteegden EE, McCarthy JJ, and Peterson CA (2015). Inducible depletion of satellite cells in adult, sedentary mice impairs muscle regenerative capacity without affecting sarcopenia. Nat. Med 21, 76–80. [PubMed: 25501907]

Gilbert PM, Havenstrite KL, Magnusson KE, Sacco A, Leonardi NA, Kraft P, Nguyen NK, Thrun S, Lutolf MP, and Blau HM (2010). Substrate elasticity regulates skeletal muscle stem cell self-renewal in culture. Science 329, 1078–1081. [PubMed: 20647425]

Hamed M, Khilji S, Chen J, and Li Q (2013). Stepwise acetyltransferase association and histone acetylation at the Myod1 locus during myogenic differentiation. Sci. Rep 3, 2390. [PubMed: 23928680]

Heinz S, Benner C, Spann N, Bertolino E, Lin YC, Laslo P, Cheng JX, Murre C, Singh H, and Glass CK (2010). Simple combinations of lineage-determining transcription factors prime cis-regulatory elements required for macrophage and B cell identities. Mol. Cell 38, 576–589. [PubMed: 20513432]

Iezzi S, Cossu G, Nervi C, Sartorelli V, and Puri PL (2002). Stage-specific modulation of skeletal myogenesis by inhibitors of nuclear deacetylases. Proc. Natl. Acad. Sci. USA 99, 7757–7762. [PubMed: 12032356]

Iezzi S, Di Padova M, Serra C, Caretti G, Simone C, Maklan E, Minetti G, Zhao P, Hoffman EP, Puri PL, and Sartorelli V (2004). Deacetylase inhibitors increase muscle cell size by promoting myoblast recruitment and fusion through induction of follistatin. Dev. Cell 6, 673–684. [PubMed: 15130492]

Jeoung NH, Rahimi Y, Wu P, Lee WNP, and Harris RA (2012). Fasting induces ketoacidosis and hypothermia in PDHK2/PDHK4-double-knockout mice. Biochem. J 443, 829–839. [PubMed: 22360721]

Kim B, Kim J-S, Yoon Y, Santiago MC, Brown MD, and Park J-Y (2013). Inhibition of Drp1-dependent mitochondrial division impairs myogenic differentiation. Am. J. Physiol. Regul. Integr. Comp. Physiol 305, R927–R938.

Lala-Tabbert N, Fu D, and Wiper-Bergeron N (2016). Induction of CCAAT/enhancer-binding protein β expression with the phosphodiesterase inhibitor isobutylmethylxanthine improves myoblast engraftment into dystrophic muscle. Stem Cells Transl. Med 5, 500–510. [PubMed: 26941360]

Lepper C, Partridge TA, and Fan C-M (2011). An absolute requirement for Pax7-positive satellite cells in acute injury-induced skeletal muscle regeneration. Development 138, 3639–3646. [PubMed: 21828092]

Li B, and Dewey CN (2011). RSEM: accurate transcript quantification from RNA-Seq data with or without a reference genome. BMC Bioinformatics 12, 323. [PubMed: 21816040]

Li H, and Durbin R (2009). Fast and accurate short read alignment with Burrows-Wheeler transform. Bioinformatics 25, 1754–1760. [PubMed: 19451168]

Lin S, and Garcia BA (2012). Examining histone posttranslational modification patterns by high-resolution mass spectrometry. Meth. Enzymol 512, 3–28. [PubMed: 22910200]

Lu J, McKinsey TA, Zhang CL, and Olson EN (2000). Regulation of skeletal myogenesis by association of the MEF2 transcription factor with class II histone deacetylases. Mol. Cell 6, 233–244. [PubMed: 10983972]

Marchildon F, Lala N, Li G, St-Louis C, Lamothe D, Keller C, and Wiper-Bergeron N (2012). CCAAT/enhancer binding protein beta is expressed in satellite cells and controls myogenesis. Stem Cells 30, 2619–2630. [PubMed: 23034923]

McLean CY, Bristor D, Hiller M, Clarke SL, Schaar BT, Lowe CB, Wenger AM, and Bejerano G (2010). GREAT improves functional interpretation of cis-regulatory regions. Nat. Biotechnol 28, 495–501. [PubMed: 20436461]

Megeney LA, Kablar B, Garrett K, Anderson JE, and Rudnicki MA (1996). MyoD is required for myogenic stem cell function in adult skeletal muscle. Genes Dev. 10, 1173–1183. [PubMed: 8675005]

Mink S, Haenig B, and Klempnauer KH (1997). Interaction and functional collaboration of p300 and C/EBPbeta. Mol. Cell. Biol 17, 6609–6617. [PubMed: 9343424]

Moussaieff A, Rouleau M, Kitsberg D, Cohen M, Levy G, Barasch D, Nemirovski A, Shen-Orr S, Laevsky I, Amit M, et al. (2015). Glycolysis-mediated changes in acetyl-CoA and histone acetylation control the early differentiation of embryonic stem cells. Cell Metab. 21, 392–402. [PubMed: 25738455]

Muir AR, Kanji AH, and Allbrook D (1965). The structure of the satellite cells in skeletal muscle. J. Anat 99, 435–444. [PubMed: 5857082]

Nerlov C (2007). The C/EBP family of transcription factors: a paradigm for interaction between gene expression and proliferation control. Trends Cell Biol. 17, 318–324. [PubMed: 17658261]

Pala F, Di Girolamo D, Mella S, Yennek S, Chatre L, Ricchetti M, and Tajbakhsh S (2018). Distinct metabolic states govern skeletal muscle stem cell fates during prenatal and postnatal myogenesis. J. Cell Sci 131, jcs212977. [PubMed: 30054310]

Patel MS, Nemeria NS, Furey W, and Jordan F (2014). The pyruvate dehydrogenase complexes: structure-based function and regulation. J. Biol. Chem 289, 16615–16623. [PubMed: 24798336]

Pliner HA, Packer JS, McFaline-Figueroa JL, Cusanovich DA, Daza RM, Aghamirzaie D, Srivatsan S, Qiu X, Jackson D, Minkina A, et al. (2018). Cicero predicts *cis*-regulatory DNA interactions from single-cell chromatin accessibility data. Mol. Cell 71, 858–871.e8. [PubMed: 30078726]

Polesskaya A, Naguibneva I, Fritsch L, Duquet A, Ait-Si-Ali S, Robin P, Vervisch A, Pritchard LL, Cole P, and Harel-Bellan A (2001). CBP/p300 and muscle differentiation: no HAT, no muscle. EMBO J 20, 6816–6825. [PubMed: 11726517]

Porpiglia E, Samusik N, Ho ATV, Cosgrove BD, Mai T, Davis KL, Jager A, Nolan GP, Bendall SC, Fantl WJ, and Blau HM (2017). High-resolution myogenic lineage mapping by single-cell mass cytometry. Nat. Cell Biol 19, 558–567. [PubMed: 28414312]

Puri PL, Avantaggiati ML, Balsano C, Sang N, Graessmann A, Giordano A, and Levrero M (1997a). p300 is required for MyoD-dependent cell cycle arrest and muscle-specific gene transcription. EMBO J. 16, 369–383. [PubMed: 9029156]

Puri PL, Sartorelli V, Yang X-J, Hamamori Y, Ogryzko VV, Howard BH, Kedes L, Wang JYJ, Graessmann A, Nakatani Y, and Levrero M (1997b). Differential roles of p300 and PCAF acetyltransferases in muscle differentiation. Mol. Cell 1, 35–45. [PubMed: 9659901]

Puri PL, Iezzi S, Stiegler P, Chen TT, Schiltz RL, Muscat GE, Giordano A, Kedes L, Wang JY, and Sartorelli V (2001). Class I histone deacetylases sequentially interact with MyoD and pRb during skeletal myogenesis. Mol. Cell 8, 885–897. [PubMed: 11684023]

Rahimi Y, Camporez J-PG, Petersen MC, Pesta D, Perry RJ, Jurczak MJ, Cline GW, and Shulman GI (2014). Genetic activation of pyruvate dehydrogenase alters oxidative substrate selection to induce skeletal muscle insulin resistance. Proc. Natl. Acad. Sci. USA 111, 16508–16513. [PubMed: 25368185]

Rasmussen BB, and Phillips SM (2003). Contractile and nutritional regulation of human muscle growth. Exerc. Sport Sci. Rev 31, 127–131. [PubMed: 12882478]

Rodgers JT, King KY, Brett JO, Cromie MJ, Charville GW, Maguire KK, Brunson C, Mastey N, Liu L, Tsai C-R, et al. (2014). mTORC1 controls the adaptive transition of quiescent stem cells from G0 to G(Alert). Nature 510, 393–396. [PubMed: 24870234]

Ryall JG, Dell'Orso S, Derfoul A, Juan A, Zare H, Feng X, Clermont D, Koulnis M, Gutierrez-Cruz G, Fulco M, and Sartorelli V (2015). The NAD^+-dependent SIRT1 deacetylase translates a metabolic switch into regulatory epigenetics in skeletal muscle stem cells. Cell Stem Cell 16, 171–183. [PubMed: 25600643]

Sacco A, Doyonnas R, Kraft P, Vitorovic S, and Blau HM (2008). Self-renewal and expansion of single transplanted muscle stem cells. Nature 456, 502–506. [PubMed: 18806774]

Sambasivan R, Yao R, Kissenpfennig A, Van Wittenberghe L, Paldi A, Gayraud-Morel B, Guenou H, Malissen B, Tajbakhsh S, and Galy A (2011). Pax7-expressing satellite cells are indispensable for adult skeletal muscle regeneration. Development 138, 3647–3656. [PubMed: 21828093]

Seale P, Sabourin LA, Girgis-Gabardo A, Mansouri A, Gruss P, and Rudnicki MA (2000). Pax7 is required for the specification of myogenic satellite cells. Cell 102, 777–786. [PubMed: 11030621]

Shea KL, Xiang W, LaPorta VS, Licht JD, Keller C, Basson MA, and Brack AS (2010). Sprouty1 regulates reversible quiescence of a self-renewing adult muscle stem cell pool during regeneration. Cell Stem Cell 6, 117–129. [PubMed: 20144785]

Silberstein L, Webster SG, Travis M, and Blau HM (1986). Developmental progression of myosin gene expression in cultured muscle cells. Cell 46, 1075–1081. [PubMed: 3530499]

Sin J, Andres AM, Taylor DJR, Weston T, Hiraumi Y, Stotland A, Kim BJ, Huang C, Doran KS, and Gottlieb RA (2016). Mitophagy is required for mitochondrial biogenesis and myogenic differentiation of C2C12 myoblasts. Autophagy 12, 369–380. [PubMed: 26566717]

Soleimani VD, Yin H, Jahani-Asl A, Ming H, Kockx CE, van Ijcken WF, Grosveld F, and Rudnicki MA (2012). Snail regulates MyoD binding-site occupancy to direct enhancer switching and differentiation-specific transcription in myogenesis. Mol. Cell 47, 457–468. [PubMed: 22771117]

Stacpoole PW, Henderson GN, Yan Z, and James MO (1998). Clinical pharmacology and toxicology of dichloroacetate. Environ. Health Perspect 106 (Suppl 4), 989–994. [PubMed: 9703483]

Tanaka KK, Hall JK, Troy AA, Cornelison DDW, Majka SM, and Olwin BB (2009). Syndecan-4-expressing muscle progenitor cells in the SP engraft as satellite cells during muscle regeneration. Cell Stem Cell 4, 217–225. [PubMed: 19265661]

Tang AH, and Rando TA (2014). Induction of autophagy supports the bioenergetic demands of quiescent muscle stem cell activation. EMBO J. 33, 2782–2797. [PubMed: 25316028]

Taylor GCA, Eskeland R, Hekimoglu-Balkan B, Pradeepa MM, and Bickmore WA (2013). H4K16 acetylation marks active genes and enhancers of embryonic stem cells, but does not alter chromatin compaction. Genome Res. 23, 2053–2065. [PubMed: 23990607]

von Maltzahn J, Jones AE, Parks RJ, and Rudnicki MA (2013). Pax7 is critical for the normal function of satellite cells in adult skeletal muscle. Proc. Natl. Acad. Sci. USA 110, 16474–16479. [PubMed: 24065826]

Wang Z, Zang C, Rosenfeld JA, Schones DE, Barski A, Cuddapah S, Cui K, Roh T-Y, Peng W, Zhang MQ, and Zhao K (2008). Combinatorial patterns of histone acetylations and methylations in the human genome. Nat. Genet 40, 897–903. [PubMed: 18552846]

Wellen KE, Hatzivassiliou G, Sachdeva UM, Bui TV, Cross JR, and Thompson CB (2009). ATP-citrate lyase links cellular metabolism to histone acetylation. Science 324, 1076–1080. [PubMed: 19461003]

Wright WE, Sassoon DA, and Lin VK (1989). Myogenin, a factor regulating myogenesis, has a domain homologous to MyoD. Cell 56, 607–617. [PubMed: 2537150]

Young NL, DiMaggio PA, Plazas-Mayorca MD, Baliban RC, Floudas CA, and Garcia BA (2009). High throughput characterization of combinatorial histone codes. Mol. Cell. Proteomics 8, 2266–2284. [PubMed: 19654425]

Yuan Z-F, Lin S, Molden RC, Cao X-J, Bhanu NV, Wang X, Sidoli S, Liu S, and Garcia BA (2015). EpiProfile Quantifies Histone Peptides With Modification by Extracting Retention Time and Intensity in High-resolution Mass Spectra. Mol. Cell Proteomics 14, 1696–1707. [PubMed: 25805797]

Zhang Y, Liu T, Meyer CA, Eeckhoute J, Johnson DS, Bernstein BE, Nusbaum C, Myers RM, Brown M, Li W, and Liu XS (2008). Model-based analysis of ChIP-seq (MACS). Genome Biol. 9, R137. [PubMed: 18798982]

Zheng Y, Thomas PM, and Kelleher NL (2013). Measurement of acetylation turnover at distinct lysines in human histones identifies long-lived acetylation sites. Nat. Commun 4, 2203. [PubMed: 23892279]

Zurlo F, Larson K, Bogardus C, and Ravussin E (1990). Skeletal muscle metabolism is a major determinant of resting energy expenditure. J. Clin. Invest 86, 1423–1427. [PubMed: 2243122]

Highlights

- Histone acetylation levels change with muscle stem cell states during regeneration
- Mitochondrial glucose utilization determines overall histone acetylation levels
- PDH activity controls histone acetylation and myogenic differentiation potential
- PDK2 and PDK4 are required for skeletal muscle regeneration *in vivo*

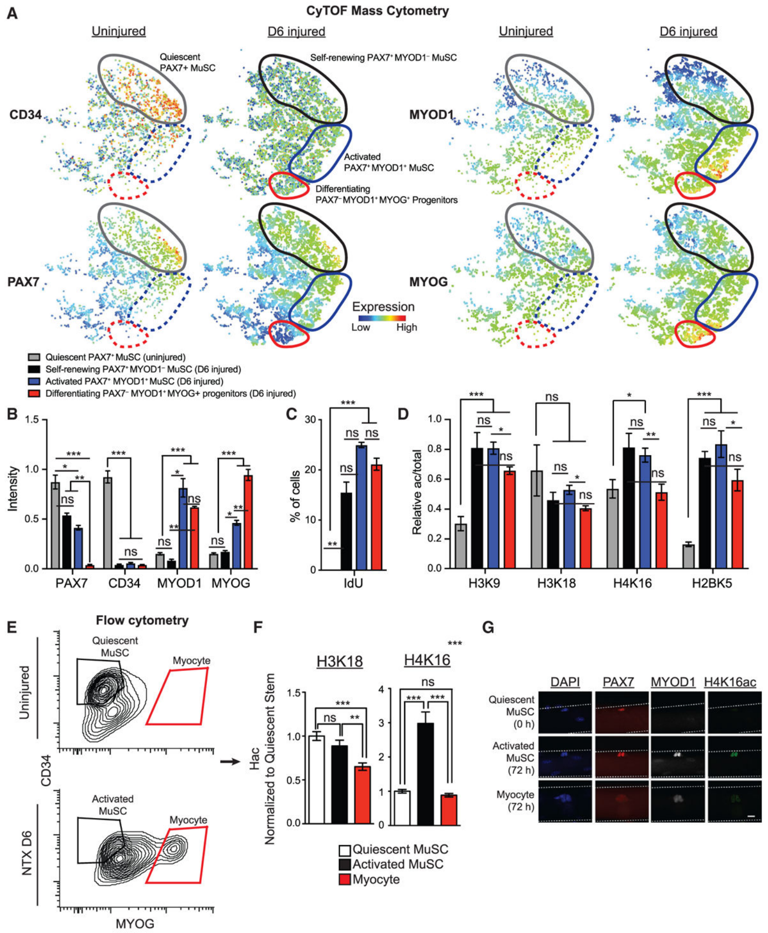

Figure 1. Histone Acetylation Dynamics during Regeneration Revealed by CyTOF

(A) Visualization of t-distributed stochastic neighbor embedding (viSNE) plot of uninjured and injured (D6 after notexin injection) muscle. Sca1/CD31/CD11b/ CD45$^-$ (Lin$^-$) α7-integrin$^+$ cells were clustered based on PAX7, MYOD1, and MYOG (Myogenin). viSNE plots of combined biological replicates (n = 3) for each time point shown. Color scale shows CD34, PAX7, MYOD1, or MYOG normalized expression. Significance determined using one-way ANOVA with Tukey's test for multiple comparisons across samples (injured and uninjured), and repeated-measures ANOVA was used for comparisons between Activated or Self-Renewing Stem and Differentiated subsets within biological samples. Subsets outlined are as follows: (a) quiescent PAX7$^+$CD34$^+$MYOD$^-$ MuSCs (D0), gray; (b) self-renewing PAX7$^+$CD34$^-$MYOD$^-$ MuSCs (D6), black; (c) activated PAX7$^+$MYOD$^+$ MuSCs (D6), blue; and (d) differentiating PAX7$^-$MYOD$^+$MYOG$^+$ progenitors (D6), red. (B) Expression of PAX7, CD34, MYOD1, and MYOG in subsets in (A).

(C) IdU incorporation subsets in (A).

(D) Histone acetylation normalized for total histone H3 content in subsets outlined in (A).

(E) Representative contour plot of CD34 versus MYOG at D0 and D6. Cells are Lin$^-$α7-integrin$^+$. Quiescent (CD34$^+$MYOG$^-$), Activated (CD34^{Low}MYOG$^-$), and Differentiated (CD34^{Low}MYOG$^+$) subsets are indicated.

(F) H4K16 and H3K18 acetylation in Quiescent, Activated, and Differentiated subsets. Acetylation normalized for Quiescent MuSCs. n = 4–11 biological replicates. Significance determined using one-way ANOVA with Tukey’s test for multiple comparisons across samples (injured and uninjured), and Student’s paired t test was used for comparisons between within biological samples.

(G) Immunostaining of H4K16ac on *extensor digitorum* muscle fibers. Freshly isolated fibers were compared to those cultured for 72 h. Quiescent MuSCs identified as PAX7$^+$MYOD1$^-$, activated MuSCs as PAX7$^+$MYOD$^+$, and early differentiated progenitors as PAX7$^-$/MYOD$^+$ cells. Scale bar (white): 10 μm. Data are represented as mean ± SEM (*p < 0.05, **p < 0.01, and ***p < 0.001). See Figures S1 and S2 and Table S1.

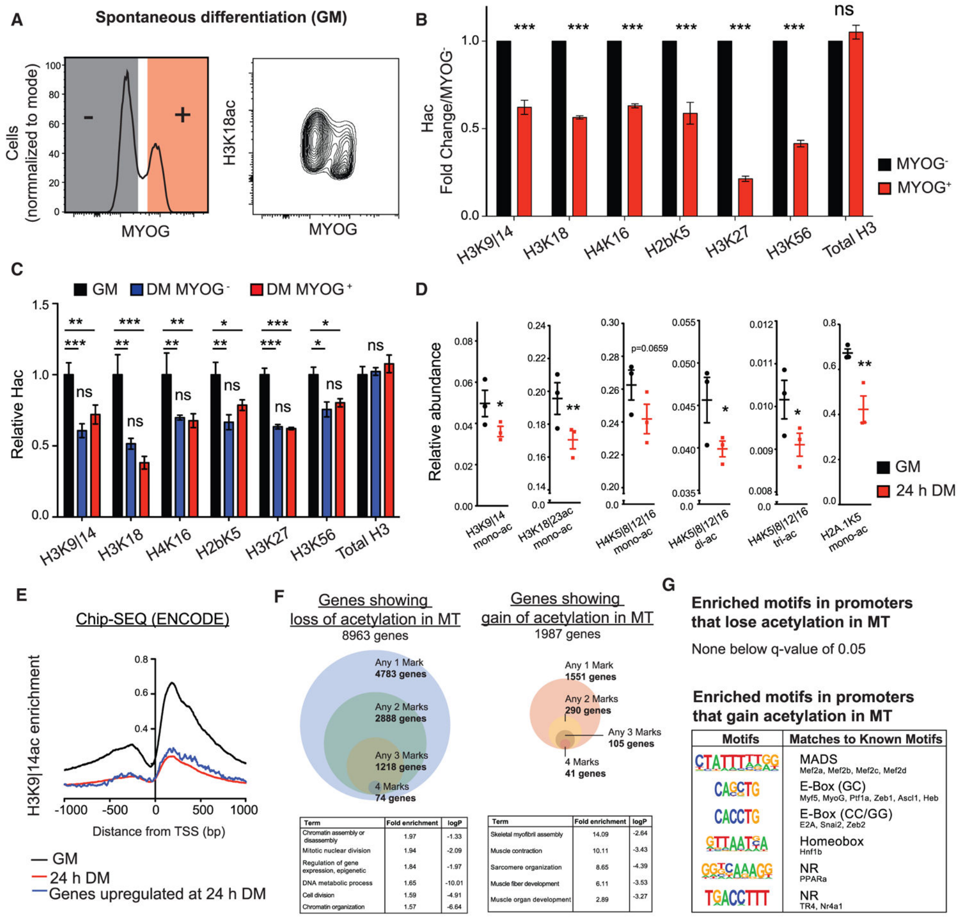

Term	Fold enrichment	logP
Chromatin assembly or disassembly	1.97	-1.33
Mitotic nuclear division	1.94	-2.09
Regulation of gene expression, epigenetic	1.84	-1.97
DNA metabolic process	1.65	-10.01
Cell division	1.59	-4.91
Chromatin organization	1.57	-6.64

Term	Fold enrichment	logP
Skeletal myofibril assembly	14.09	-2.64
Muscle contraction	10.11	-3.43
Sarcomere organization	8.65	-4.39
Muscle fiber development	6.11	-3.53
Muscle organ development	2.89	-3.27

Enriched motifs in promoters that lose acetylation in MT

None below q-value of 0.05

Enriched motifs in promoters that gain acetylation in MT

Motifs	Matches to Known Motifs
CTATTTTTGG	MADS Mef2a, Mef2b, Mef2c, Mef2d
CAGCTG	E-Box (GC) Myf5, MyoG, Ptf1a, Zeb1, Ascl1, Heb
CACCTG	E-Box (CC/GG) E2A, Snai2, Zeb2
GTTAATGA	Homeobox Hnf1b
GGTCAAAGG	NR PPARa
TGACCTTT	NR TR4, Nr4a1

Figure 2. Histone Acetylation Is Reduced in MYOG$^+$ Progenitors, and upon Induction of Myogenic Differentiation by Serum Removal, but Spares the Myogenic Program

(A) Representative histogram (MYOG) and contour plot (H3K18ac versus MYOG) of confluent, heterogeneously differentiated myoblasts in GM (~15%–30% MYOG$^+$). MYOG$^+$ and MYOG$^-$ gates are in red and black.

(B) Normalized histone acetylation or total histone H3 intensity for MYOG$^-$ versus MYOG$^+$ myoblasts within same samples. n = 3–4 biological replicates are shown. Student’s paired t test was used for comparisons.

(C) Histone acetylation in sub-confluent myoblasts in GM versus 24 h in DM. The percentage of MYOG+ cells in GM and DM was <5% and 40%–60%, respectively (Figures S3B and S3C). n = 3–4 biological replicates. Significance determined using one-way ANOVA with Tukey’s test for multiple comparisons across samples (GM and DM), and Student’s paired t test was used for comparisons between MYOG$^-$ and MYOG$^+$ cells within biological samples.

(D) Histone acetylation in GM and 24-h DM myoblasts by LC-MS/MS. Lysine acetylation calculated as a fraction relative to each histone peptide (relative abundance). Histone peptides analyzed from the following, left to right: H3 9–17; H3 18–26; H4 4–17; and H2A1–11. n = 3 biological replicates were run on a mass spectrometer three independent times. For statistical comparisons, two-way ANOVA was used with matching for experimental runs.

(E) Enrichment of H3K9|14 acetylation across the genome for a 2-kbp window around transcriptional start sites (TSSs). ChIP-sequencing and gene expression data used from the Mouse ENCODE Consortium (GSE36023).

(F) Histone acetylation ChIP-sequencing from C212 myoblasts and myotubes (D7 of differentiation) analyzed from Blum et al. (2012) and Asp et al. (2011) (H3K9, H4K12, H3K18, and H3K27ac, respectively). Genes associated with each peak were identified within a 2-kb window around the TSS. A total of 8,963 genes showed reduced histone acetylation on any one or more mark in myotubes (left) and 1,967 genes were identified with increased histone acetylation in myotubes (right). Shown are the number of genes associated with loss or gain of any one, two, three, or all four histone acetylation marks. Gene set enrichment for genes shown below.

(G) HOMER Motif enrichment analysis of promoters of genes associated with loss (top) or increase (bottom) of histone acetylation on one or more marks. No significant motifs identified for genes with loss of acetylation. Promoters of genes with increased histone acetylation enriched for MADS, E-Box, Homeobox, and NR (nuclear receptor) consensus motifs.

Data are represented as mean ± SEM (*p < 0.05, **p < 0.01, and ***p < 0.001). See also Figure S3.

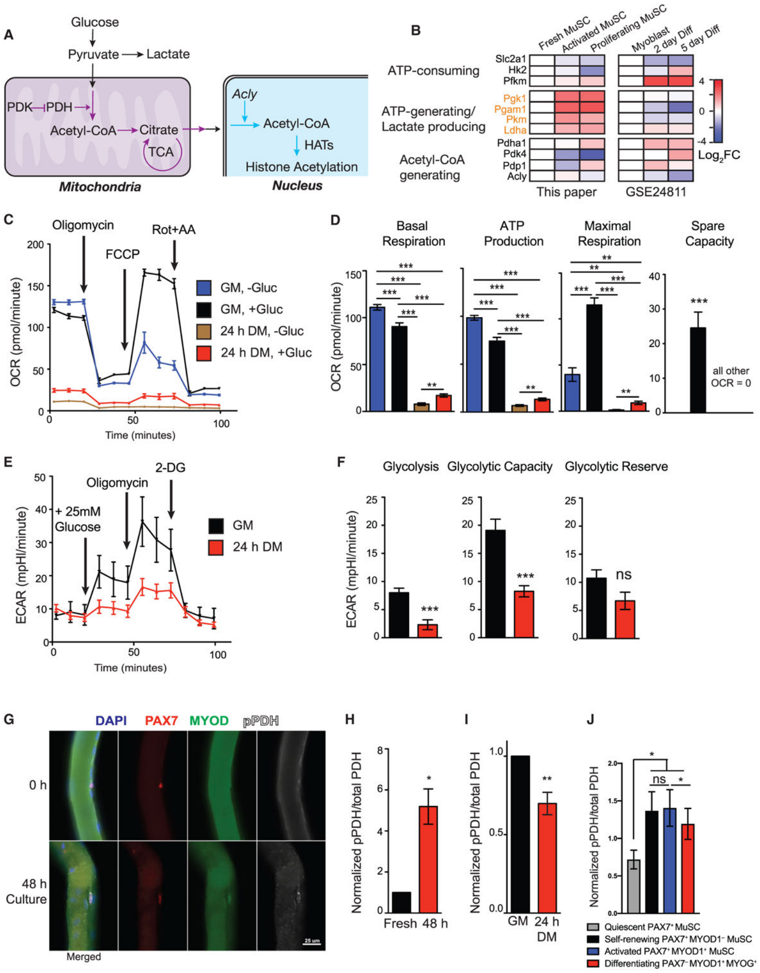

Figure 3. Myogenic Fate Corresponds to Distinct Glycolytic States

(A) Flux from glucose to histone acetylation.

(B) Expression of glycolytic genes in freshly isolated and 2-day hydrogel cultured MuSCs and primary myoblasts grown on collagen-coated plastic. Color scale shows Log_2Fold compared to mean TPM (transcripts per million) of fresh MuSCs (left) or proliferating myoblasts (right). Genes in orange indicate ATP-generating phase/lactate-producing stage of glycolysis. Right, Log_2Fold change shown for MuSC-derived myoblasts versus day 2 versus day 5 of induced differentiation of published microarray data (GSE24811; Soleimani et al., 2012). For statistical comparisons of all replicates of RNA-seq data, see Table S2.

(C–F) Bioenergetic profile of confluent primary myoblasts in growth media (GM) or after 24 h in differentiation media (DM). Oxygen consumption rate (OCR) and extracellular acidification rate (ECAR) were measured using a Seahorse XF96 extracellular flux analyzer using the Mitochondrial Stress or Glycolytic Stress kits. n = 5–8 biological replicates. One-way ANOVA with Tukey's test for multiple comparisons used.

(C) Oxygen consumption profile for GM (15% FBS) or 24-h DM (5% horse serum) myoblasts with or without 25 mM glucose.

(D) Basal respiration, ATP production, maximal respiration, and spare capacity for GM and DM ± 25 mM glucose.

(E) Glycolytic stress profile for GM versus 24-h DM.

(F) Glycolytic rate, capacity, and reserve for GM and DM myoblasts.

(G) Immunostaining for pPDH, PAX7, and MYOD1 on isolated single fibers from *soleus* fixed immediately after isolation, or after 48 h in culture in GM.

(H) pPDH/PDH by flow cytometry for freshly isolated versus 48-h cultured MuSCs on hydrogels. n = 4 independent experiments. Student's paired t test was used for statistical comparison.

(I) Quantification of pPDH/PDH for primary myoblasts in GM versus 24-h DM. n = 3 independent experiments. Student's paired t test was used for statistical comparisons.

(J) pPDH/PDH of quiescent, self-renewing, and activated ($MYOD^-$ and $MYOD^+$) MuSCs, and $MYOG^+$ differentiating progenitors CyTOF (as characterized in Figure 1). n = 3 biological replicates, one-way ANOVA with Tukey's test for multiple comparisons used for comparisons against quiescent MuSCs, and repeated-measures ANOVA used to compare activated versus differentiated subsets within biological replicates.

Data are represented as mean ± SEM (*$p < 0.05$, **$p < 0.01$, and ***$p < 0.001$). See also Figure S4 and Table S2.

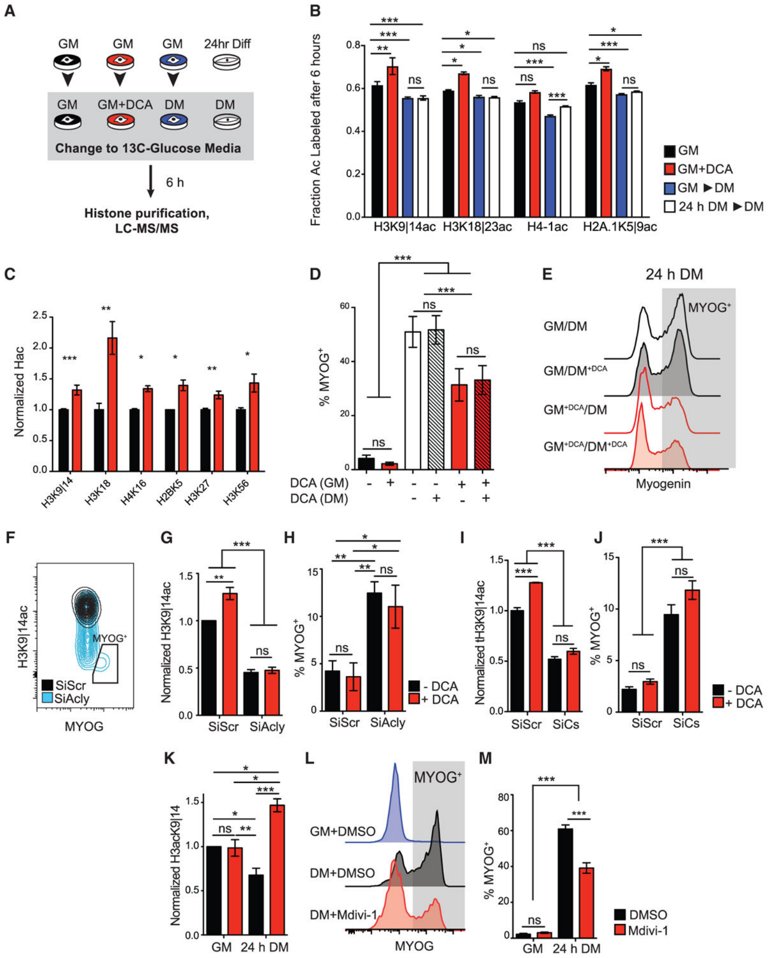

Figure 4. Glucose Flux toward Histone Acetylation Decreases upon Myogenic Differentiation

(A) Scheme of ^{13}C glucose labeling. Sub-confluent primary myoblasts in GM were switched to GM or GM + DCA (10 mM) or DM for 6 h. In parallel, 24-h differentiated, confluent myoblasts were switched to labeled DM for 6 h. ^{13}C glucose was added to a final concentration of 25 mM. n = 3 biological replicates used for each condition.

(B) Quantification of ^{13}C incorporation by LC-MS/MS as outlined in (A). Incorporation of labeled glucose quantified as fraction of labeled (+2-Da shift) over total acetylation (labeled + unlabeled) for each mark. Incorporation on singly acetylated lysines was analyzed: H3 9–17; H3 18–26; H4 4–17; and HH2A 4–11. n = 3 biological replicates were run on a mass spectrometer three independent times. For comparisons, two-way ANOVA was used with matching for each experimental run.

(C) H3K9|14, H3K18, H4K16, H2bK5, H3K27, and H3K56 acetylation of proliferating myoblasts after 24-h DCA, normalized for untreated controls. n = 3 biological replicates; statistics calculated by Student's paired t test.

(D) Effect of DCA on differentiation. Cells were untreated (−/−), treated with DCA only in DM (−/+), treated in GM but not DM (+/−), or treated with DCA in both GM and DM (+/+). Differentiation quantified as percentage positive for MYOG. n = 5–6 biological replicates.

(E) Histogram of MYOG in myoblasts differentiated for 24 h following DCA treatment in GM, DM, or both (−/−, −/+, +/−, +/+). MYOG^{+} gate in gray.

(F) Contour plot of MYOG versus H3K9|14ac following 72-h treatment with scrambled siRNA or si*Acly*. MYOG+ gate outlined.

(G) H3K9|14 histone acetylation following si*Acly* or SiScramble. DCA or vehicle added after 24-h knockdown and treatment continued for 48 h, for a total of 72-h siRNA treatment. n = 3.

(H) MYOG$^+$ quantification following si*Acly* or SiScramble, +/− DCA as described in (G). n = 3.

(I) H3K9|14 acetylation following si*Cs* or SiScramble, +/− DCA by flow cytometry. n = 3.

(J) MYOG$^+$ quantification following si*Cs* or SiScramble, +/− DCA. n = 3.

(K) H3K9|14 histone acetylation following DMSO (vehicle) or 20 μM Mdivi-1 treatment of myoblasts in GM or DM for 24 h.

(L) Histogram, MYOG$^+$ after 24-h treatment with DMSO or 20 μM Mdivi-1 in GM or DM.

(M) MYOG$^+$ quantification of myoblasts in GM or DM treated with DMSO or Mdivi-1 for 24 h. n = 3.

Data are represented as mean ± SEM ($*p < 0.05$, $**p < 0.01$, and $***p < 0.001$). Unless otherwise indicated, significance was calculated by one-way ANOVA with Tukey's test for multiple comparisons for n = 3 biological replicates. See also Figure S5.

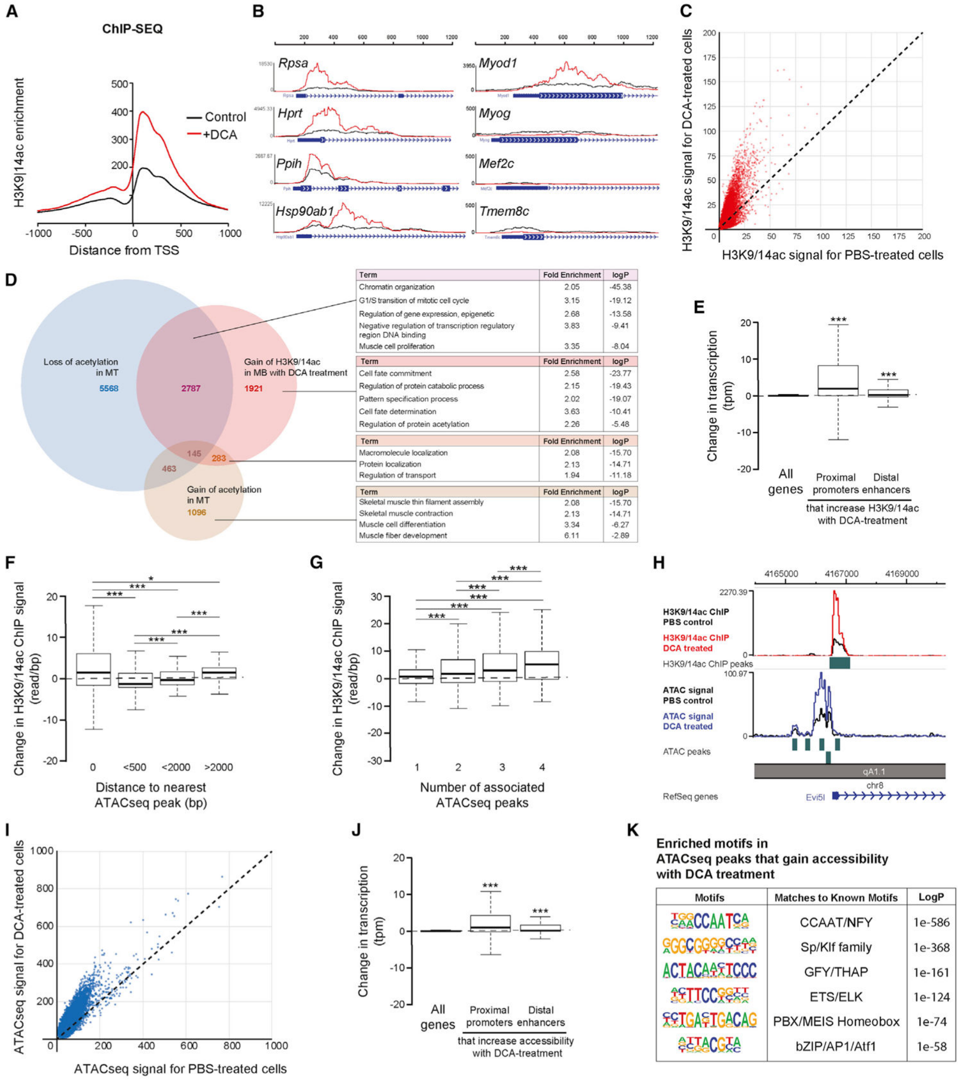

Term	Fold Enrichment	logP
Chromatin organization	2.05	-45.38
G1/S transition of mitotic cell cycle	3.15	-19.12
Regulation of gene expression, epigenetic	2.68	-13.58
Negative regulation of transcription regulatory region DNA binding	3.83	-9.41
Muscle cell proliferation	3.35	-8.04

Term	Fold Enrichment	logP
Cell fate commitment	2.58	-23.77
Regulation of protein catabolic process	2.15	-19.43
Pattern specification process	2.02	-19.07
Cell fate determination	3.63	-10.41
Regulation of protein acetylation	2.26	-5.48

Term	Fold Enrichment	logP
Macromolecule localization	2.08	-15.70
Protein localization	2.13	-14.71
Regulation of transport	1.94	-11.18

Term	Fold Enrichment	logP
Skeletal muscle thin filament assembly	2.08	-15.70
Skeletal muscle contraction	2.13	-14.71
Muscle cell differentiation	3.34	-6.27
Muscle fiber development	6.11	-2.89

Motifs	Matches to Known Motifs	LogP
TGGCCAATCA	CCAAT/NFY	1e-586
GGGCGGGGCCAA	Sp/Klf family	1e-368
ACTACAACTCCC	GFY/THAP	1e-161
ACTTCCGGTT	ETS/ELK	1e-124
CCTGACTGACAG	PBX/MEIS Homeobox	1e-74
ATTACGTA	bZIP/AP1/Atf1	1e-58

Figure 5. Genomic Characterization of Glucose-Metabolism Mediated Histone Acetylation

(A) ChIP-sequencing of H3K9|14 acetylation of proliferating myoblasts in GM ± DCA for 24 h. Enrichment shown for a ±1-kb window around TSSs.

(B) Genomic tracks for representative housekeeping (left) and myogenic genes (right).

(C) ChIP-sequencing signal for peaks in control versus DCA treated myoblasts. The dotted line indicates slope of 1 (x = y).

(D) Gene set enrichment analysis of genes associated with increased ChIP-sequencing peak signal in DCA versus control myoblasts. Overlap with genes with gain or loss of at least one histone acetylation mark in myotube versus myoblasts (see Figure 2F) shown.

(E) Average change in expression in absolute transcripts per million (TPM) following DCA treatment. Change in expression of all genes was compared with those with increased ChIP-sequencing peaks following DCA treatment in proximal promoters (±2 kb) or distal enhancer (−100 kb). Statistical comparison was made versus average change in TPM over all genes (0).

(F) Comparison of ChIP-sequencing and ATAC-seq. Chromatin accessibility by ATAC-seq was assayed in myoblasts in GM ± DCA. Change in ChIP-sequencing signal shown as a function of distance to nearest ATAC-seq peak.

(G) Comparison of ChIP-sequencing and ATAC-seq. Chromatin accessibility by ATAC-seq was assayed in myoblasts in GM with or without DCA treatment. Change in ChIP-sequencing signal is shown as a function of number of associated ATAC-seq peaks.

(H) Genomic track of H3K9|14 ChIP-sequencing and ATAC-seq peaks for control and DCA-treated myoblasts.

(I) ATAC-seq signal of peaks in control versus DCA treated myoblasts. The dotted line shows slope of 1 ($x = y$).

(J) Change in expression in absolute transcripts per million (TPM) following DCA treatment. Expression of all genes was compared with those with increased ATAC-seq peaks following DCA treatment in proximal promoters (±2 kb) or distal enhancer (−100 kb). Statistical comparison made versus average change in TPM over all genes (0).

(K) HOMER motif enrichment analysis of genes that show increased accessibility by ATAC-seq following DCA treatment.

Data are represented as mean ± SEM (*$p < 0.05$, **$p < 0.01$, and ***$p < 0.001$). Unless otherwise indicated, significance was calculated by one-way ANOVA with Tukey’s test for multiple comparisons. See also Table S3.

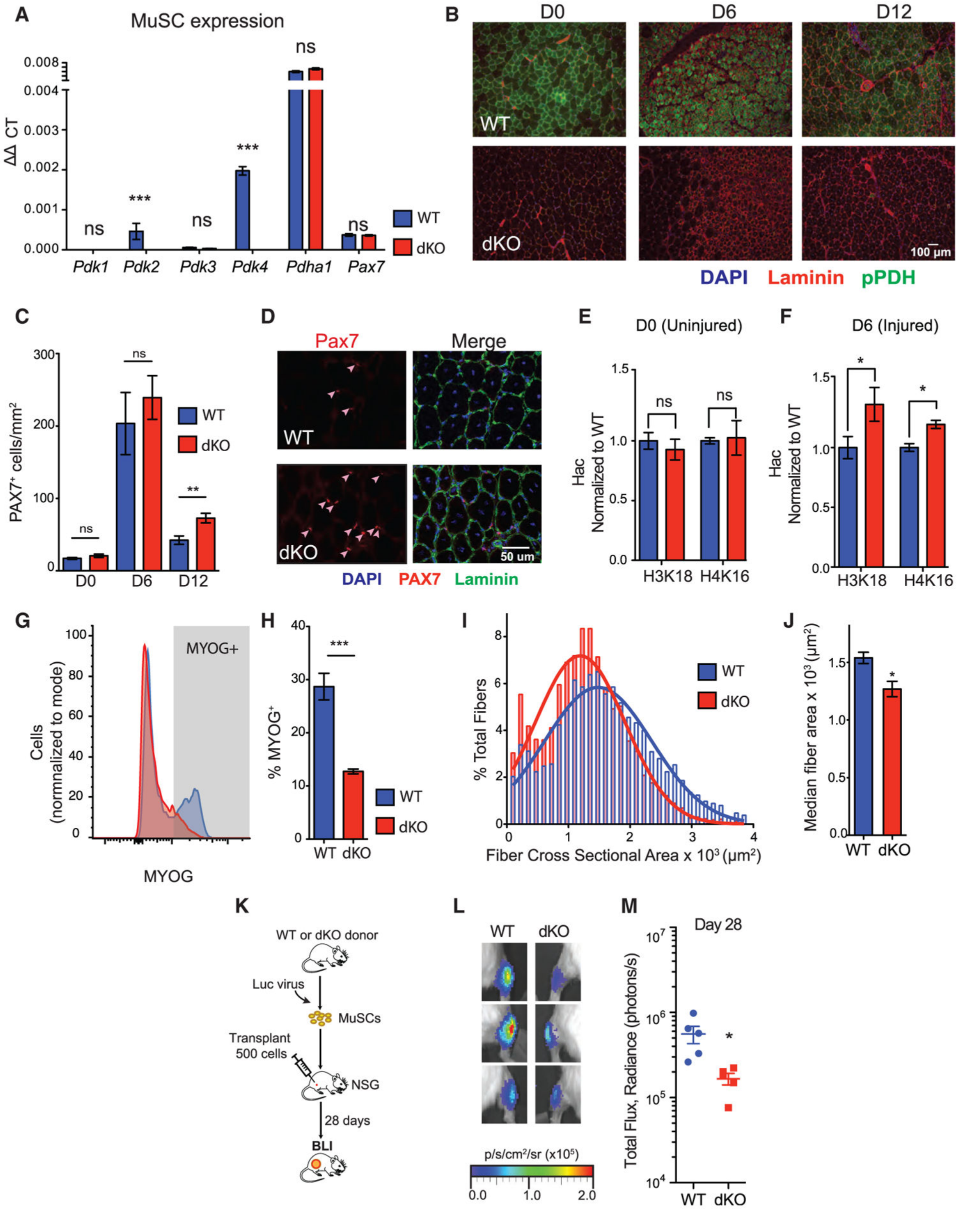

Figure 6. PDK dKO Mice Show Muscle Regeneration Defects and MuSC-Specific Histone Acetylation and Engraftment Capacity

(A) Real-time qPCR of *Pdk*(1-4), *Pdhal*, and *Pax7* expression in cultured MuSCs isolated from WT or dKO animals. n = 3 biological replicates.

(B) Immunohistochemistry for pPDH in WT and dKO animals at D0, or D6 and D12 after injury by notexin injection.

(C) Quantification of Pax7^{+} cells per area (1 mm^{2}) at D0, D6, and D12. n = 4–6 animals per time point.

(D) Representative image of Pax7^{+} MuSCs in of WT and dKO muscle at D12. DAPI, Laminin co-staining.

(E) H3K18 and H4K16 acetylation by flow cytometry for uninjured (D0) MuSCs ($Lin^{-}\alpha7$-integrin^{+}CD34^{+}MYOG^{-}). Histone acetylation normalized for uninjured WT controls in each experiment. n = 4–10 animals.

(F) H3K18 and H4K16 acetylation for injured (D6) MuSCs ($Lin^{-}\alpha7$-integrin^{+}CD34^{+}MYOG^{-}). Histone acetylation normalized for injured WT controls in each experiment. n = 3–12 animals.

(G) Histogram of MYOG^{+} cells within $Lin^{-}\alpha7$-integrin^{+} population at D6 after injury.

(H) MYOG^{+} quantification of cells as described in (G). n = 3.

(I) Histogram of fiber cross-sectional area in dKO and WT, D12 after injury.

(J) Median fiber cross-sectional area of WT and dKO at D12 after injury. n = 3 animals.

(K) Transplant assay. MuSCs were isolated from WT or dKO donors, and transduced with a Luciferase reporter virus. After 24 h, 500 cells were transplanted into irradiated NSG recipient mice. MuSCs from WT and PDK mice were transplanted into contralateral legs to minimize biological variability.

(L) BLI signal for dKO and WT; images shown for same animal.

(M) BLI signal of engrafted MuSCs 28 days after transplantation, calculated as radiance (photons/second). n = 5.

Student’s unpaired t test was used for all statistical comparisons. Data are represented as mean ± SEM (*$p < 0.05$, **$p < 0.01$, and ***$p < 0.001$). See also Figure S6.

KEY RESOURCES TABLE

REAGENT or RESOURCE	**SOURCE**	**IDENTIFIER**
Antibodies		
Mouse monoclonal anti Pax7	Santa Cruz	Catalog# sc-81648; RRID:AB_2159836
Mouse monoclonal anti Myogenin	BD Biosciences	Catalog# 556358; RRID:AB_396383
Rabbit polyclonal anti Myogenin, Clone M-225	Santa Cruz	Catalog# sc-576; RRID:AB_2148908
Rabbit polyclonal anti Myosin Heavy Chain (H-300)	Santa Cruz	Catalog# sc-20641; RRID:AB_2235573
Rat polyclonal anti Laminin, Clone A5	EMD Millipore	Catalog# 05-206; RRID:AB_309655
Rabbit polyclonal anti Ki67	Abcam	Catalog# ab66155; RRID:AB_1140752
Rabbit polyclonal anti Cleaved Caspase-3	Cell Signaling	Catalog# 9661; RRID:AB_2341188
Rabbit polyclonal anti phospho-PDH (Ser293)	Abcam	Catalog# ab92696; RRID:AB_10711672
Mouse monoclonal anti-PDH E1 alpha subunit	Abcam	Catalog# ab110330; RRID:AB_10858459
Rabbit polyclonal anti-acetyl Histone H3 (raised against the first 20 residues of H3; designated as H3K9|14ac)	EMD Millipore	Catalog #06-599; RRID:AB_2115283
Rabbit polyclonal anti-H4K16ac (Clone EPR1004)	Abcam	Catalog# ab109463; RRID:AB_10858987
Mouse monoclonal anti-H3K9 (Clone AH3-120)	Abcam	Catalog# ab12179; RRID:AB_298910
Rabbit polyclonal anti-H3K18ac	Abcam	Catalog # ab1191; RRID:AB_298692
Rabbit polyclonal anti-H2bK5ac	Abcam	Catalog# ab40886; RRID:AB_732916
Rabbit polyclonal anti-H3K56	Abcam	Catalog# ab71956; RRID:AB_10861799
Rabbit polyclonal anti H3K27	Abcam	Catalog# ab4729; RRID:AB_2118291
Rabbit polyclonal anti histone H3	Abcam	Catalog# ab1791; RRID:AB_302613
Rat monoclonal anti CD11b (Clone M1/70)	BD Biosciences	Catalog# 553309; RRID:AB_394773
Rat monoclonal anti CD45 (Clone 30F11)	BD Biosciences	Catalog# 553078; RRID:AB_394608
Rat monoclonal anti Sca1 (Clone E13-161.7)	BD Biosciences	Catalog# 553334; RRID:AB_394790
Rat monoclonal anti CD31 (Clone 390)	eBiosciences	Catalog# 13-0311-82; RRID:AB_466420
Rat monoclonal anti integrin-α_7 (clone R2F2), PE conjugated	AbLab	Catalog# 10ST215
Rat monoclonal CD34-eFluor660 (clone RAM34)	eBioscience,	Catalog # 50-0341-82; RRID:AB_10596826
Rabbit polyclonal anti Fis1	Biovision	Catalog #3491R-100; RRID:AB_2102530
Antibodies and conjugation metals used for CyTOF experiments		Table S1
Chemicals, Peptides, and Recombinant Proteins		
4',6 diamidino-2-phenylindole (DAPI)	Life Technologies	Catalog# D1306
Wheat Germ Agglutinin (WGA), AlexFluor 647	Thermo Fisher	Catalog# W32466
7-aminoactinomycin D (7-AAD)	Thermo Fisher	Catalog# A1310
Potassium dichloroacetate	Sigma-Aldrich	Catalog# 348082
D-Luciferin	Caliper Life Sciences	Catalog# 122796
Collagenase	Sigma-Aldrich	Catalog# C0130
Dispase II	Sigma-Aldrich	Catalog# 04942078001
Notexin	Latoxan	Catalog# L8104
Streptavidin Microbeads	Miltenyi Biotech	Catalog# 130-048-101
D-Glucose (U-13C)	Cambridge Isotope Laboratories	Catalog# CLM-1396
MitoTracker Deep Red FM	Thermo Fisher	Catalog# M224-26

REAGENT or RESOURCE	**SOURCE**	**IDENTIFIER**
Critical Commercial Assays		
Ovation RNA-Seq System V2 Kit	NuGEN	Catalog# 7102-08
TruSEQ RNA Library Preparation Kit v2	Illumina	Catalog# RS-122-2101
Nextera DNA Library Preapration Kit	Illumina	Catalog# FC-121-1030
XF Cell Mito Stress Test Kit	Agilent	Catalog# 103015-100
XF Cell Glyco Stress Test Kit	Agilent	Catalog# 103020-100
Deposited Data		
Raw and analyzed RNASeq, H3ac and ATACSeq data	This paper	GEO:GSE129280
C2C12 myoblast and myocyte, H3ac ChIP-SEQ	ENCODE/Caltech	GEO: GSE36023
C2C12 myoblast and myotube, H4K12, H3K9 and H3K18	Asp et al., 2011	GEO:GSE25308
C2c12 myoblast and myotube, H3K27	Blum et al., 2012	GEO:GSE37525
Experimental Models: Cell Lines		
Mouse: Primary myoblasts	This paper	n/a
Experimental Models: Organisms/Strains		
Mouse: C57BL/6J	Jackson Laboratories	000664
Mouse: C57Bl6/J: PDK2/PDK4 double knockout	Robert Harris (Indiana University)	Jeoung et al., 2012
Mouse: NOD.Cg-*Prkdc*^{scid} *Il2rg*^{tm1Wjl}/SzJ (NSG)	Jackson Laboratories	005557
Recombinant DNA		
Lentivirus Luc-IRES-GFP		N/A
Sequence-Based Reagents		
ChIP-qPCR Primer: Tmem8c-F ATGGCCTCCAT GTAGAAACG	This paper	N/A
ChIP-qPCR Primer: Tmem8c-R TTGTAGCCAAA CTGCTCCTG	This paper	N/A
ChIP-qPCR Primer: Myh3-F CTCACCAAGGTCT GGTTCGT	This paper	N/A
ChIP-qPCR Primer: Myh3-R CAGCAGTTGTGG ACGTATGG	This paper	N/A
ChIP-qPCR Primer: Myogenin-F AGCGCAGGC TCAAGAAAGT	This paper	N/A
ChIP-qPCR Primer: Myogenin-R CTTTAGGCA GCCGCTGGT	This paper	N/A
ChIP-qPCR Primer: Mef2a-F TCCTCTCGGCT TCCTCTCTT	This paper	N/A
ChIP-qPCR Primer: Mef2a-R TGTCCATGACA AACCCTTCA	This paper	N/A
ChIP-qPCR Primer: Myod1-F CGCCTGAGCA AAGTGAATG	This paper	N/A
ChIP-qPCR Primer: Myod1-R CAGGATCTCC ACCTTGGGTA	This paper	N/A
ChIP-qPCR Primer: Myf5-F AGGCCCACATG AGGCAGT	This paper	N/A
ChIP-qPCR Primer: Myf5-R CGGAGCACACA AAGCTGAG	This paper	N/A
ChIP-qPCR Primer: Pax7-F F: CCTGGAGGGT GCCATCTC	This paper	N/A
ChIP-qPCR Primer: Pax7-R R: GCTTCCCCCT GGAAGGTAA	This paper	N/A

REAGENT or RESOURCE	SOURCE	IDENTIFIER
ChIP-qPCR Primer: Rpsa-F TGGTTGGTGTTG GAGTGCTA	This paper	N/A
ChIP-qPCR Primer: Rpsa-R GTGCAGGGTCAG TCAGTCCT	This paper	N/A
ChIP-qPCR Primer: Hsp90-F TTTTGGACTAAGA AAGGGACGA	This paper	N/A
ChIP-qPCR Primer: Hsp90-R CGCTTCGTAATT ACCGCATT	This paper	N/A
ChIP-qPCR Primer: Ppih-F AGACGCAACACTC AGCTCAC	This paper	N/A
ChIP-qPCR Primer: Ppih-R CTTATAGCCCTCC CGAGACC	This paper	N/A
Acly targeting SiRNA (SiGenome) SMARTpool	Dharmacon	Catalog# M-040092-00-0005
Citrate Synthase targeting SiRNA (SiGenome) SMARTpool	Dharmacon	Catalog# M-059581-01-0005
Software and Algorithms		
Flowjo	FlowJo, LLC 2013-2016	https://www.flowjo.com/
Graphpad Prism	GraphPad Software, Inc, 2016	https://www.graphpad.com/
Metamorph Image Analysis Software	Molecular Devices	https://www.moleculardevices.com/
R	R development core team, 2014	https://www.r-project.org
STAR	Dobin et al., 2013	https://github.com/alexdobin/STAR/releases
BWA	Li and Durbin, 2009	http://bio-bwa.sourceforge.net/
RSEM	Li and Dewey, 2011	https://github.com/bli25broad/RSEM_tutorial
DESeq2	Anders and Huber, 2010	http://bioconductor.org/packages/release/bioc/html/DESeq2.html
Living Image v.4.5	Perkin Elmer, 2015	https://www.perkinelmer.com/
EpiProfile	Yuan et al., 2015	N/A
GREAT	McLean et al., 2010	http://great.stanford.edu/public/html/index.php
MACS2	Zhang et al., 2008	https://github.com/taoliu/MACS
BEDTOOLS		https://bedtools.readthedocs.io/en/latest/
HOMER	Heinz et al., 2010	http://homer.ucsd.edu/homer/